

A comprehensive numerical investigation of the impact behaviour of an offshore wind turbine blade due to impact loads during installation

Amrit Shankar Verma^{a,b,*}, Nils Petter Vedvik^c, Zhen Gao^{a,b,d}

^a*Department of Marine Technology, Norwegian University of Science and Technology (NTNU), Norway*

^b*Centre for Marine Operations in Virtual Environments (SFI MOVE), NTNU, Norway*

^c*Department of Mechanical and Industrial Engineering, NTNU, Norway*

^d*Centre for Autonomous Marine Operations and Systems (SFF AMOS), NTNU, Norway*

Abstract

For installing offshore wind turbines into deep waters, use of floating crane vessels is essential. One of the major challenges is their sensitivity to wave-induced vessel and crane tip motions, which can cause the impact of lifted components like blades and nacelle with nearby structures. The impact loads on fibre composite wind turbine blades are critical as several complex damage modes, capable of affecting the structural integrity, are developed. Planning of such installation tasks therefore requires response-based operational limits that consider impact loads on the blade along with their damage quantification. The research area considering the impact behaviour of the lifted blade is novel, and thus, the paper identifies vessel, blade and lifting parameters that determine impact/contact scenarios. Furthermore, for a case in which a lifted blade with its leading edge impacts the tower, a numerical modelling technique is presented in Abaqus/Explicit, and a comprehensive damage assessment of the blade and an investigation of the impact dynamics and energy evolution are performed. Sensitivity studies for two distinct blade designs and two different impact locations are considered. The results show that 7-20% of the impact energy is absorbed as damage in the blade, whereas the majority dissipates as rigid-body motions of the blade after the impact. The findings of the study highlight the requirement for advanced installation equipment, such as active tugger lines, to prevent successive impacts of wind turbine blades during installation.

Keywords: Offshore wind turbine blade, contact/impact, finite element method, marine operation, composite structure, floating crane vessel.

1. Introduction

- ¹ One of the most sustainable sources of energy, owing to its plentiful existence, is wind energy [1, 2, 3].
- ² As a result, land-based wind turbines have been used to generate cleaner energy for many decades.

*Corresponding author

Email addresses: amrit.s.verma@ntnu.no (Amrit Shankar Verma), nils.p.vedvik@ntnu.no (Nils Petter Vedvik), zhen.gao@ntnu.no (Zhen Gao)



(a)



(b)

Figure 1: Offshore installation vessels (a) Jack-up crane vessel, source: [9] (b) Floating crane vessel, source: [10]

3 Additionally, offshore wind turbines are in high demand because they present several advantages relative
 4 to land-based turbines. Some of the benefits include availability of higher wind speeds, low turbulence
 5 intensities, the possibility of having larger turbines because they are far from human societies and, finally,
 6 ease of transportation [2]. Nevertheless, the assembly and installation phases for offshore turbines are
 7 costly, with recent studies showing that they constitute approximately 10-20% of the CAPEX cost [2, 4, 5],
 8 compared to only 2% for land-based turbines [2].

9 To reduce the cost of energy and make offshore turbines more economical, the offshore wind industry
 10 plans to deploy turbines with increased power ratings in deeper water and far from shore [1, 4, 6, 7].
 11 An increase in the power ratings of turbines enables an offshore farm to satisfy given power capacity
 12 requirements with fewer wind turbine units. This is expected to reduce the cost of installation, as there
 13 will be fewer total turbine units to be installed, and the project will thus be more profitable. However,
 14 these types of turbines are large in size and pose safety issues during installation. The challenge is due
 15 to the components of the turbines, such as blades and the nacelle (gearbox, generator), that are sensitive
 16 and require significant precision while being lifted using offshore crane vessels [8].

17 Currently, offshore wind turbines are installed using jack-up crane vessels (fig. 1 (a)) in water depths
 18 up to 30-50 m [3]. These vessels provide a stable platform for installation because there is little differential
 19 movement of the vessel and the lifted object due to the load-bearing jacked-up legs [2, 3]. However, to
 20 satisfy the industry's demand for installing offshore wind turbines in even deeper waters, use of floating
 21 crane vessels is essential (fig. 1(b)). Floating crane vessels, unlike jack-up vessels, are sensitive to wave-
 22 induced vessel and crane tip motions and, in critical cases, are vulnerable to movement of ballast or cargo
 23 [11]. The vessel and the lifted object display combined dynamics, and the motions of the vessel, especially
 24 those excited by rotation about its longitudinal and transverse axis, develop significant responses in the

25 lifted object. This causes high impact risks of the hoisted object with the nearby structures. Moreover,
26 when performing dynamic lifts using a floating crane vessel, the maximum rate at which the object is
27 hoisted, which is determined by the winch speed [11], is also a critical element. Hoisting the lifted object
28 while the level of the deck of the vessel continuously rises and falls due to wave-induced loads causes
29 large motion of the lifted object. This can cause the lifted object to hit the deck or any equipment on
30 the vessel. **The shape of the lifted object is also a critical element during lifting. For example, the wind**
31 **turbine blade, which is a slender object, when lifted using the floating crane vessel at high altitude leaves**
32 **limited space between the crane boom and hook, and the blade could hit the boom [11].** Thus, from the
33 above discussion, it is clear that the motions arising during lifting operations, especially using floating
34 crane vessels, could cause impact/contact of the lifted component of a turbine with surrounding structures.
35 These impact risks are critical for the lifted object from a structural perspective, as these structures are
36 not originally designed for resisting impact loads during the temporary phases of installation.

37 The effect of impact-induced loads on a fibre composite wind turbine blade are more serious compared
38 to steel components such as transition pieces and monopiles [4, 7]. The steel structures are inherently
39 ductile in nature, and most of the energy during the impact is dissipated in the plastic phase or work
40 hardening phase before the material fails [12]. Again, such damage to the steel structures is quite discrete
41 and visually detectable, with the possibility of predicting the consequence based on visible dent or cracks.
42 A wind turbine blade, on the other hand, is comprised of composite sandwich materials, which provide
43 a high stiffness-to-weight ratio, including excellent in-plane structural performance [7, 12, 13]. However,
44 these materials are weak in their off-axis direction and are sensitive to impact loads [13]. Several intricate
45 and interacting damage modes can develop [12, 13, 14], and they are not always detectable via visual
46 inspection; however, such damage can grow under operational loads [15] and can cause global structural
47 failure of the blade. In addition, damage of varying sizes, positions and locations in the blade could
48 affect the residual strength and performance of the blade in a multitude of manners, and judging its
49 criticality is thus difficult [4, 6, 7]. Haselbach et al. [16] found that delamination arising close to the
50 surface of the laminate of the blade at the suction side has a more adverse effect than delamination near
51 the middle layers of the laminate of the blade. **Overall, the impact loads on wind turbine blades are**
52 **critical, and therefore, planning of such installation tasks requires response-based operational limits that**
53 **consider impact loads on the blade along with their damage quantification.**

54 Verma et al. [6] proposed a structural response-based approach for estimating limiting sea states and
55 operability for a blade lifting task using a floating crane vessel; see fig. 2. **The methodology consists**
56 **of four interrelated steps: (1) global response analysis of the installation system for estimation of the**
57 **motion of the vessel and lifted blade for various sea states; (2) finite element analysis to investigate the**

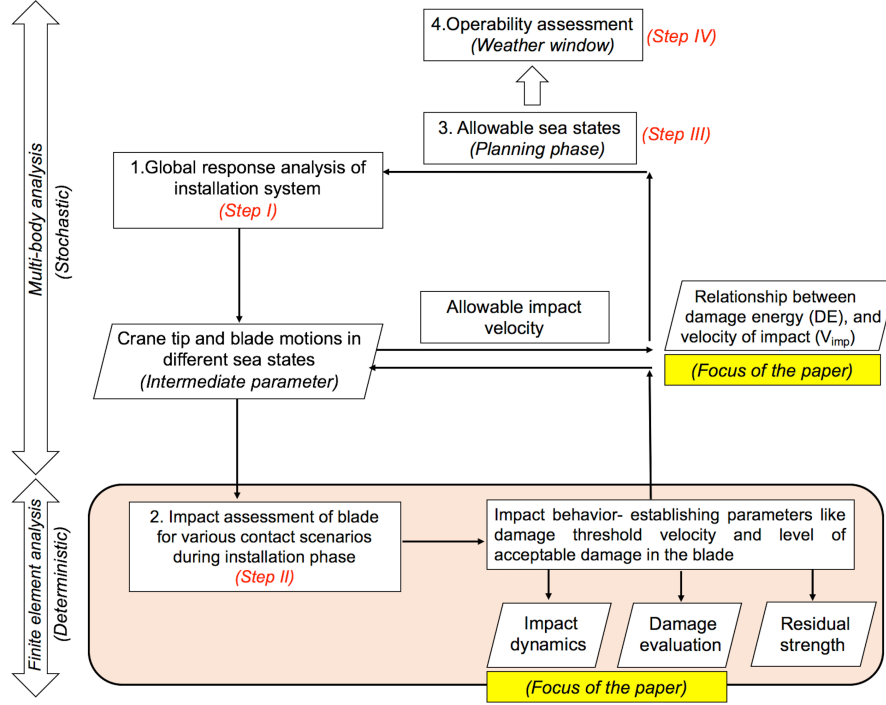


Figure 2: Explicit structural response-based methodology [4, 6]

58 impact behaviour of the lifted blade for different impact scenarios; (3) assessment of allowable sea states,
 59 in which characteristic values are compared with strength parameters; and, finally, (4) estimation of the
 60 operability of the task for a given offshore site. Note that one of the sub-steps for assessing the allowable
 61 impact velocity is to establish a relationship between the damage energy (DE) and impact velocity (V_{imp}).
 62 In this paper, we focus explicitly on the second step addressing the impact behaviour of the blade during
 63 installation, where emphasis is placed on the investigation of the impact dynamics and damage evaluation
 64 using finite element analysis. The parameters that determine impact/contact scenarios for the lifted blade
 65 during installation are identified. Furthermore, for a case in which a lifted blade impacts the tower with
 66 its leading edge, a numerical modelling technique is implemented in Abaqus/Explicit. Sensitivity studies
 67 for two distinct blade designs and two different impact locations are performed. Further, an attempt is
 68 made to understand the motion of blade after the impact, which will explicitly indicate the possibility of
 69 successive impacts of the blade with surrounding structures. Finally, a relationship between the damage
 70 energy (DE) and impact velocity (V_{imp}) is established. The remainder of the paper proceeds as follows.
 71 Sections 2 and 3 present parameters that determine impact/contact scenarios and discuss the material and
 72 modelling methods for a case study considered in this work. Section 4 presents and discusses the results
 73 for impact dynamics and damage assessment obtained for blade impact. Further, section 5 concludes the
 74 paper followed by section 6 which discusses the limitation and future work.

75 **2. Contact scenario, contact region and numerical modelling method**

76 *2.1. Parameters determining contact/impact scenario*

77 Damage assessment of a composite structure due to impact loads is not a recent development. Scientists have been examining this research topic for several years, especially in aerospace and defense applications [7, 14, 17]. However, the problem of a lifted offshore wind blade suffering impact during 78 installation tasks because of crane tip and blade motions is a novel research area.

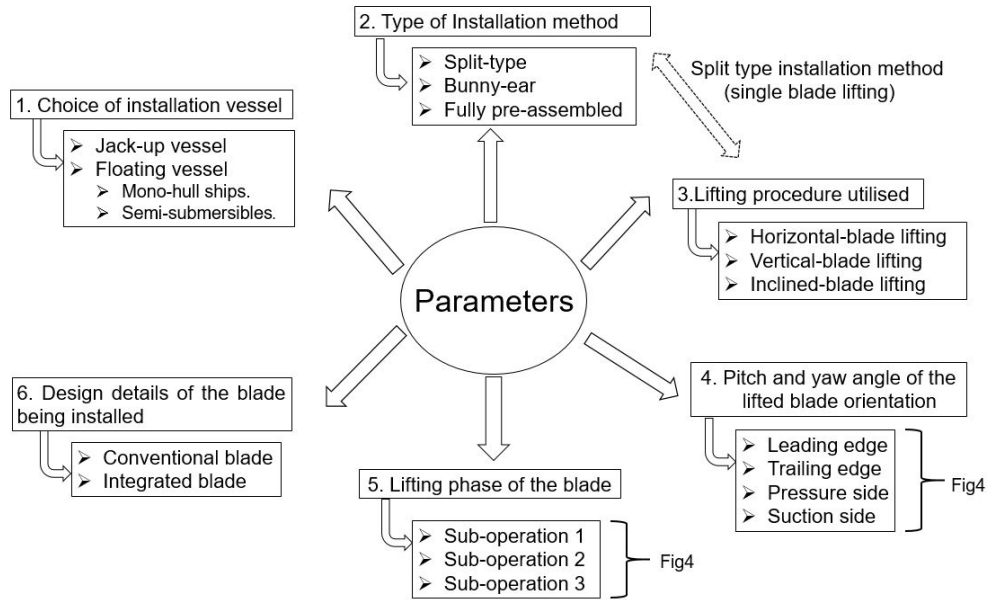


Figure 3: Parameters deciding impact/contact scenarios for single blade lifting

81 Such a problem would depend on the contact scenario in question as the blade is lifted from the deck
 82 during its lifting phase and is finally mated to the hub. Thus, throughout the hoisting phase, the blade
 83 undergoes various sub-phases varying with the height of the lift (fig. 4) and presents different contact
 84 scenarios depending on a few parameters. Fig. 3 lists the parameters that determine the contact/impact
 85 scenarios during the blade lifting task and the criticality of impact loads. These parameters are the (a)
 86 choice of installation vessel, (b) type of assembly method for installing offshore wind components, (c)
 87 lifting procedure, (d) pitch and yaw angle of the hoisted blade, (e) lifting phase of the blade, and (f)
 88 design details of the blade being installed. Note that all these identified parameters are applicable to
 89 blade installation using both jack-up and floating crane vessels. Further explanation of these parameters
 90 can be found in [6], in which single-blade lifting using offshore crane vessels is discussed. Among all the
 91 parameters, the lifting phase and pitch angle of the hoisted blade (figs. 3, 4) determine the impact region
 92 of the blade for a given contact scenario. For example, during the full lift-off phase of the blade, a lifting
 93 method with a pitch angle of zero degrees can cause the blade's leading edge to impact the pre-assembled

turbine tower or crane boom, whereas during the mating phase, the blade root with guide pin bolts can impact the hub [6, 7, 8]. These are well illustrated in fig. 4.

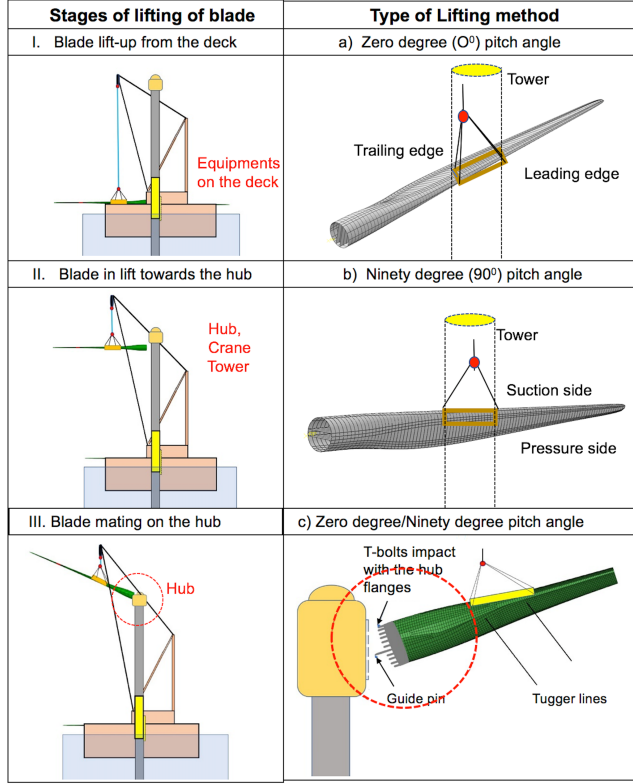


Figure 4: Different stages of blade lifting and various contact/impact region

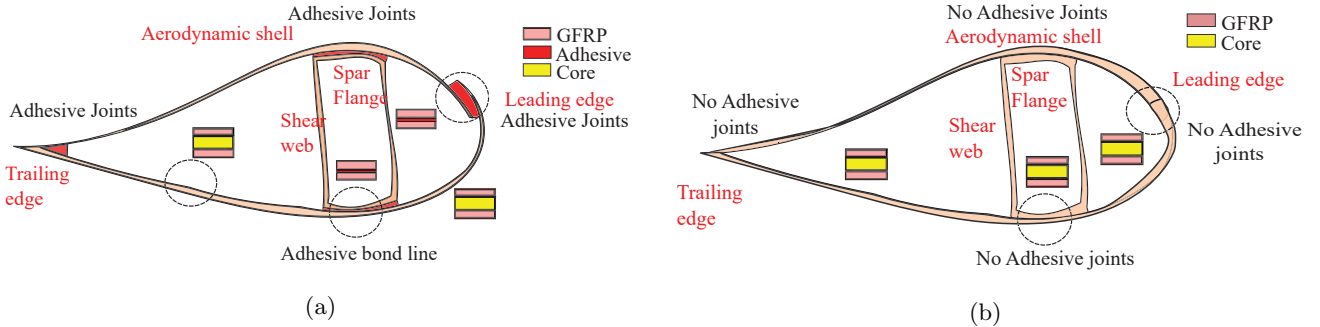


Figure 5: Types of blade design (a) Conventional blade-type (b) Integrated blade-type

One of the most important parameters from a structural point of view that decides the criticality of such impact loads is the design details of the wind turbine blade being installed. In practice, there are a wide variety of blade designs available, of which the conventional and traditional design of blades involves the construction of different subcomponents that are joined together using adhesive connections [18]. This is referred to as the ‘conventional blade-type’ in this paper (fig. 5(a)). Another important blade

101 design involves no use of adhesive connections in the blade, and the blade is constructed in a single piece.
 102 This is referred to as the ‘integrated blade-type’ in this paper [18] (fig. 5(b)). These design details of the
 103 blade are an important consideration for impact investigations, given that these blades vary structurally
 104 and thus exhibit varying impact resistance. Thus, this paper presents the numerical modelling technique
 105 and compares damage assessments for the blade based on the above two blade design types. This will be
 106 explained in more detail later in this section.

107 *2.2. Description of the chosen contact scenario and contact region considered in the study*

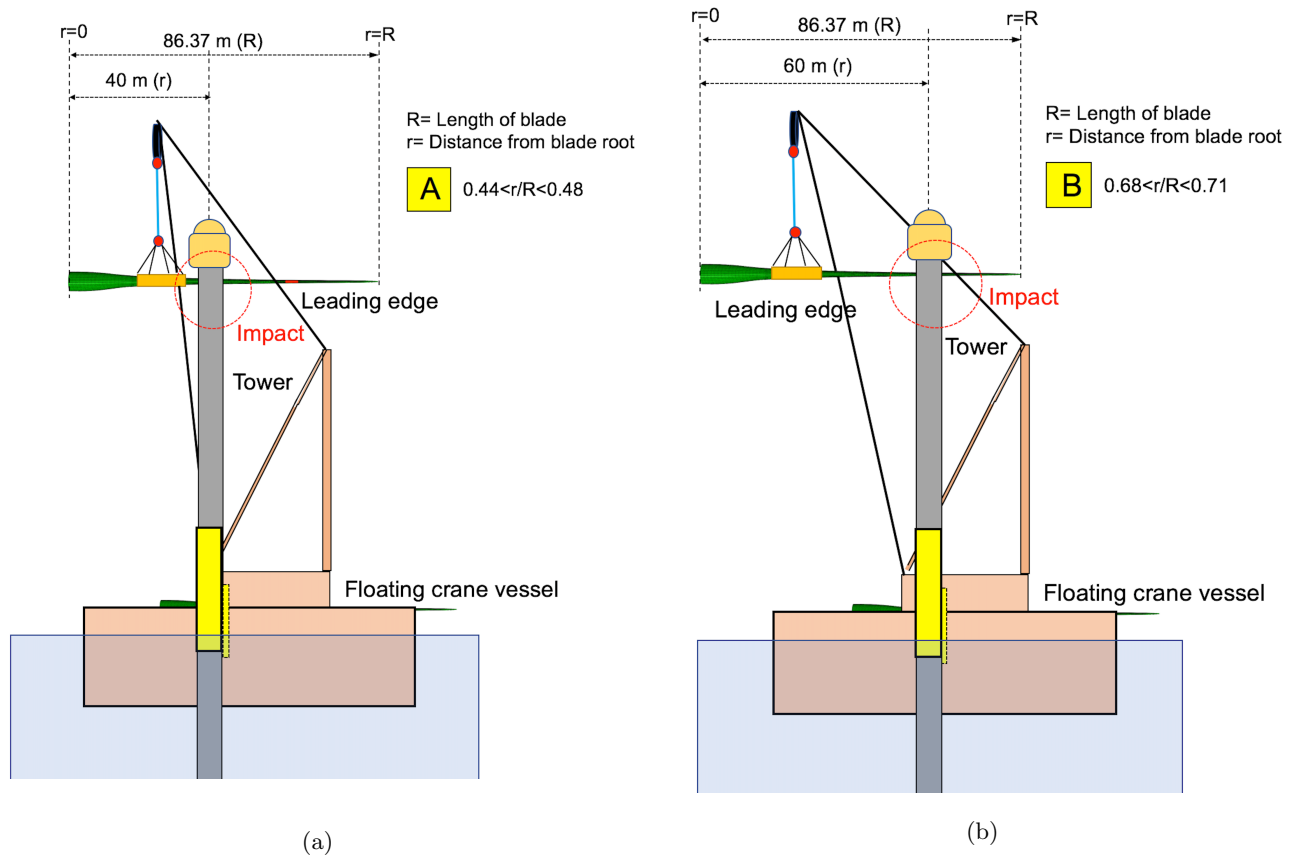


Figure 6: Contact regions considered: (a) Contact region ‘A’ ($0.44 < r/R < 0.48$) (b) Contact region ‘B’ ($0.68 < r/R < 0.71$)

108 The present paper considers the impact for one of the most critical stages of blade installation, in
 109 which the blade is in the full lift-off phase and close to the hub height (figs. 6(a)-(b)). This sub-phase
 110 is critical because the blade in this scenario is at its highest position, where the largest wind loads and
 111 largest floating vessel-induced motions are expected. Moreover, it is assumed that the blade is lifted
 112 using a horizontal single blade lifting method with zero-degree pitch angle, and thus, the relevant contact
 113 scenario to investigate is an impact of the leading edge of the blade with the tower. Two different
 114 blade designs, (a) a conventional blade-type with adhesive connections on the leading edge and (b) an

integrated blade-type with a sandwich section at the leading edge, are considered. Furthermore, the impact investigations are considered at two different regions along the leading edge: one close to the area where yoke is attached to the blade ($0.44 < r/R < 0.48$, ‘A’) and the other region near the tip of the blade ($0.68 < r/R < 0.71$, ‘B’) (figs. 6(a)-(b)). The reason for investigating two contact regions along the leading edge is because these regions vary in terms of the composite layup and have non-identical thicknesses; they thus have varying local strength and stiffness. Additionally, from a dynamic point of view, any impact closer to the tip region of the leading edge is a more-eccentric impact compared to an impact close to the yoke, and thus, the impact dynamics are expected to vary for the same impact velocity. Note that it is the motion analysis of the installation system that determines the impact velocity with which the blade suffers impact; see fig. 2. However, a global analysis of installation systems is beyond the scope of this paper, and the impact investigation using finite element analysis is considered for several impact velocities (V_x) ranging from 0.02 to 0.5 m/s. This range of velocities is reported as predominant while lifting blades using a floating crane vessel [6, 19].

2.3. Modelling method

In this paper, the DTU 10 MW reference wind turbine blade [20] is considered as the base model for impact investigations. The reference blade is originally a shell model, is 86.4 m long and has a root diameter of 5.4 m. The blade is generic in design and consists of composite and sandwich section along with load bearing spar caps and shear webs. Furthermore, the blade has only an adhesive connection modelled partially at the trailing edge, and there are no other adhesive connections either at the leading edge or at the spar cap-web assembly joint. Hence, the DTU 10 MW reference blade can be assumed to be an integrated blade-type with no specific adhesive joints. In this section, we present a numerical modelling technique based on shell elements for impact investigation of a blade based on the integrated blade-type and conventional blade-type. However, first, a brief discussion of the characteristics and limitations of the shell-element-based impact modelling of composites is presented.

Characteristics and limitations of shell-element-based impact modelling for composites:

In this study, the impact scenario involves a full-length lifted wind turbine blade impacting a tower with its leading edge. It is already known that a composite structure at full-scale length has large flexibility compared to its coupon representation, and thus, the structure stores more elastic energy due to impact [7, 21]. As a result, the entire flexibility and inertia of the structure must be considered during the finite element analysis; for this problem, the shell-element-based method is an efficient method. Note that three broad aspects [22] are required to characterise the impact investigation of a composite structure: (1) *impact responses*, which describe impact forces, impact dynamics, and energy evolutions; (2) *impact resistances*,

147 which describe the nature of damage and failure modes developed due to impact; and, finally, (3) *damage*
148 *tolerances*, which describe the residual strength of the composite after the impact. In this paper, the
149 first two aspects are the main focus of investigation for the blade impact, and thus, the discussion of the
150 shell-element-based method is focussed on impact responses and impact resistances (together termed as
151 impact behaviour).

152 Shell elements are generally utilised for modelling large composite structures with many degrees of
153 freedom. The structure's thickness dimension is considerably less than its width and length dimensions [13,
154 23, 24]. Using the shell-element-based approach, the thickness is defined as a section-specific parameter;
155 this makes the analysis cheaper [25]. Furthermore, one of the critical parameters for numerical modelling
156 of composites is the consideration of inter-laminar shear stresses. This is because for a composite, the
157 inter-laminar shear moduli are small compared to the in-plane modulus, and thus, the inter-laminar shear
158 stresses are critical. Thus, for investigation of blade impacts, the present paper considers a general-purpose
159 conventional thick shell element (S4R) [25] from the Abaqus library for impact modelling of the blade.
160 S4R elements are enforced by Mindlin-Reissner theory [25] and can estimate the inter-laminar shear
161 stresses using correction factors. These elements are 4-noded quadrilateral elements with formulation
162 suitable for analysis including large deformation and strain [25, 13]. Another important characteristic
163 of the modelling method is the possibility of defining different plies and material orientations through
164 the thickness using section integration point definition. This helps in analysing the damaged states of a
165 composite at the ply level, but at an efficient computational cost. **The utilised method also has demerits**
166 **and can influence the results obtained for the impact response and impact resistance.** In [26], it was found
167 **that shell-element based method overestimates the impact forces, and exhibited a relatively stiffer response**
168 **compared to solid elements.** Additionally, impact modelling of composites based on this technique could
169 **not discretely model an important failure mode for a composite sandwich structure, i.e., delamination and**
170 **debonding of layers.** However, it should be noted that a suitable global-local modelling technique, such
171 as a submodelling method, in which advanced material modelling is possible in the region of impact, can
172 be utilised. However, such an analysis would still require transfer of temporal and spatial displacement
173 fields from a coarser global solution based on shell elements to the driving nodes of the submodel. Thus,
174 the present paper considers the shell-element-based modelling technique sufficient to be performed at the
175 global scale.

176 *Numerical modelling method for the integrated blade-type:*

177 The parent blade derived from the DTU repository [20] is a shell model with no adhesive connection,
178 and thus, the blade represents an integrated blade-type. Note that the leading edge, which is the impact
179 region in the study, is a sandwich section. Further, the blade consists of glass fibre reinforced polymer

(GFRP) plies, and is added with balsa material as the core. The blade has 100 cross sections, with each section divided into 11 regions circumferentially. Each region is assigned with a specific composite layup plan; however, the stacking sequence is multi-directional and has triaxial, biaxial and uniaxial plies. These multi-directional plies are equivalent representations of the individual unidirectional plies, and the properties are derived based on the classical micro-mechanics equations and classical laminate theory (CLT) [20]. The reason for incorporating such smeared properties into the blade is because the objective of the reference model was to analyse the structural performance against operational loading conditions, and thus, this layup provides ease and convenience. However, the present multi-directional based formulation of layup is not suitable for impact investigation because an explicit understanding of specific plies that can be critically damaged due to impact loads is not possible.

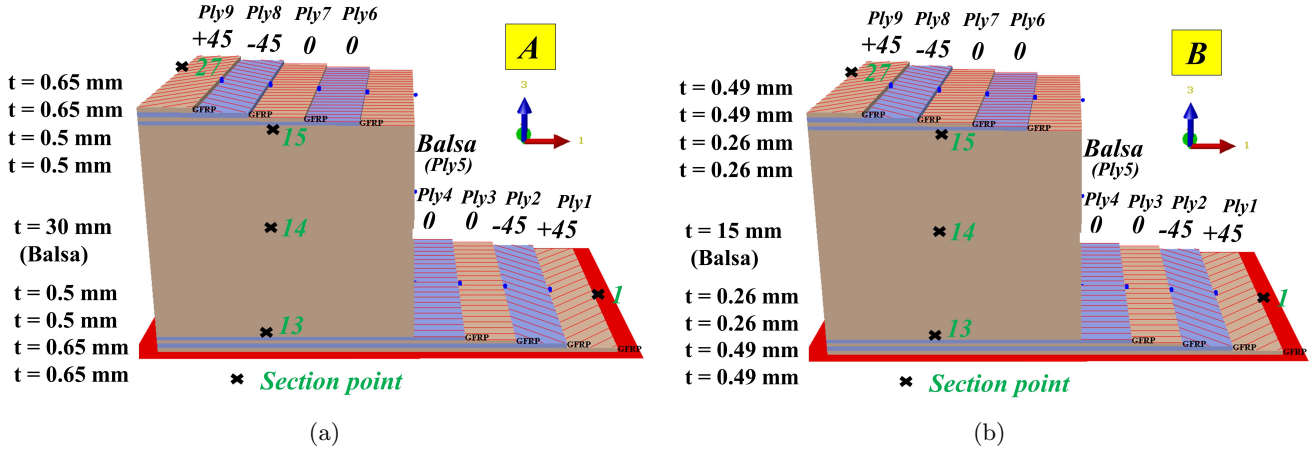


Figure 7: DTU 10 MW blade modified layup-[+45/-45/0₂/Balsa]_s at (a) contact region 'A' (b) contact region 'B'

Hence, for impact investigation, a stacking sequence based on unidirectional nomenclature is required. Thus, the original layup for the reference blade in the impact region is derived in the form of [+45/-45/0₂/Balsa]_s (figs. 7(a)-(b)). An iterative procedure is developed that calculates multi-directional plies back into their parent individual ply definitions, while considering parameters such as the thickness of the laminate at the contact region, mass of the blade and COG of the blade consistent with the parent definitions. Furthermore, to check that this modified layup in terms of individual plies does not influence the blade's global characteristics, eigenvalue analyses are performed, and the results are compared to the parent DTU 10 MW blade. Table 1 presents the eigenfrequencies for different modes, and it can be seen that the modified layup yields sound results. Furthermore, a base impact analysis is also performed on the parent and modified blades to compare the local stiffness at the contact region for a case in which the leading edge impacts the tower with an impact velocity of 0.1 m/s. It can be seen from figs. 8(a) and 8(b) that the contact-force histories and kinetic energy evolution histories are in close agreement for the parent and modified blades. Overall, these results validate that the modified layup definition is consistent

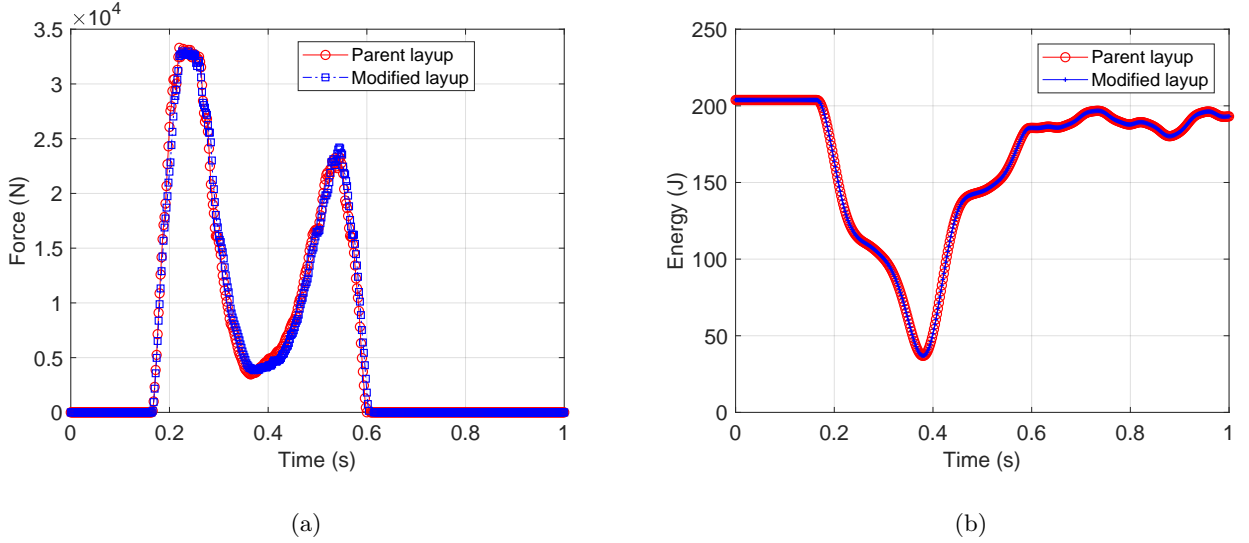


Figure 8: Comparison between modified and parent blade layup ($0.44 < r/R < 0.48$) (a) Contact force history (b) Kinetic energy evolution

Table 1: Eigenfrequency comparison for the DTU 10 MW blade with parent and modified layup

Eigen Mode	DTU Parent	DTU Modified
1st Flapwise mode [Hz]	0.617	0.613
1st Edgewise mode [Hz]	0.963	0.967
2nd Flapwise mode [Hz]	1.752	1.749
2nd Edgewise mode [Hz]	2.862	2.91
3rd Flapwise mode [Hz]	3.581	3.589
3rd Edgewise mode [Hz]	6.511	6.521

with the original parent blade layup and can thus be utilised for the impact investigation. Finally, each ply in the layup is defined with three section points, and thus, 27 section points are associated with the contact regions. Note that section point 1 corresponds to the outermost ply, which represent the shell reference surface, whereas section points 13, 14 and 15 correspond to the balsa material (Ply-5); see figs. 7(a) and 7(b).

Numerical modelling for the conventional blade-type:

Here, we present a numerical modelling method for the conventional type blade, which is still the most widely used blade type in the industry. These blade types have adhesive connections at their leading edges, where the impact is considered in this study. To model an adhesive connection and then simulate impact-induced cracks based on a fracture mechanics approach, solids and cohesive brick elements are required at the leading edge. This approach will be significantly computationally demanding and thus in this paper, we investigate impact damage on the adhesive connections of the blade based on a strength-based

approach. This can be achieved by using a stratification technique, in which adhesive material is modelled as a part of the composite layup (stacking sequence) using shell-element-based modelling. The adhesive and top and bottom composite laminates at the leading edge are defined as different layers in the layup, and failure in the adhesive layer is predicted based on a yield-based criterion such as Drucker Prager model.

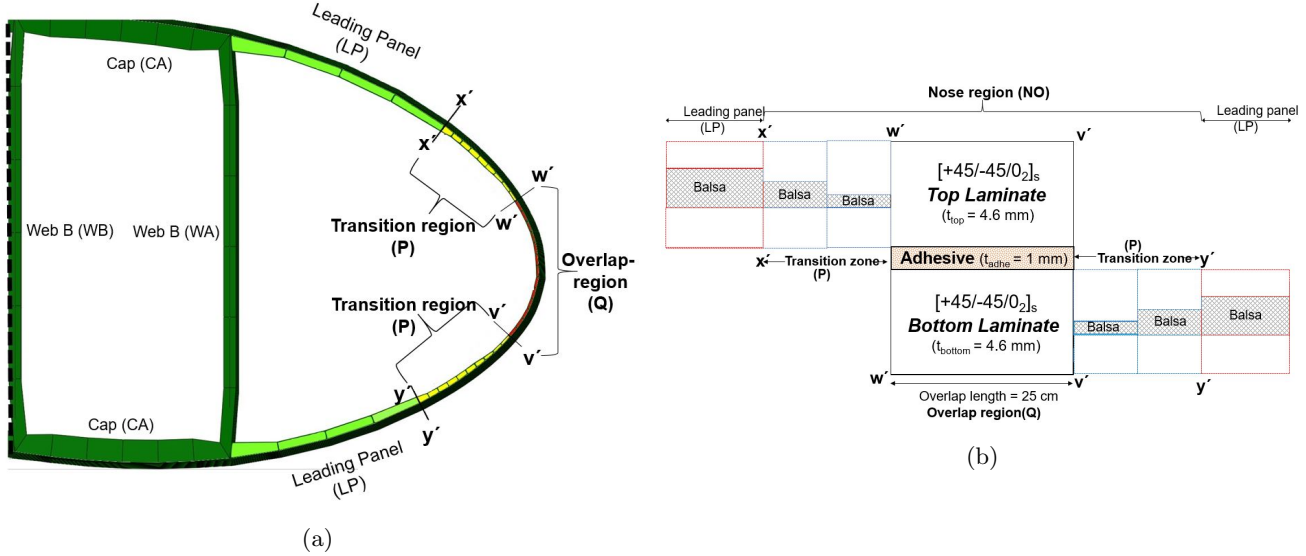


Figure 9: (a) Modelling of adhesive joint at the leading edge (b) Composite layup at the region of impact

The modelling of the adhesive joints based on a stratification technique enforces some assumptions and simplification to the problem. The first assumption is that the thickness of bond-line at the leading edge is uniform and free of imperfection. It is further assumed that the top laminate [+45/-45/0₂]_s on the suction side is single-lapped joint with the bottom laminate [+45/-45/0₂]_s on the pressure side with an adhesive material. The overlap length of the joint is uniformly varying throughout the blade length and is assumed equal to 50% of the length of the nose region (20-40 cm).

To define the adhesive connection at the leading edge of the blade, the nose section (XX-YY) is divided into two regions: transition region (P) and overlap region (Q). The overlap region (Q) (WW-VV) (fig. 9 (a)-(b)) corresponds to the region of the lap joint, and consists of composite laminate as adherends along with the adhesive material. On the other hand, the transition region of the nose (P) (XX-WW;YY-VV) aids in the gradual transitioning of the layup including balsa, and prevents any stress concentrations owing to ply drops. Note that the thickness of the balsa gradually declines from 30 mm at the leading panel (LP) to 10 mm at the end of transition region and there is no core modelled at the overlap region. The final layup for the blade at the leading edge is [+45/-45/0₂]_s-Adhesive-[+45/-45/0₂]_s, and has a total of 17 plies with a thickness of 10.2 mm at the contact region. Note that the adhesive used in this study is Araldite 2015 and is a ductile adhesive used in the blade industry. Further, the adhesive thickness varies

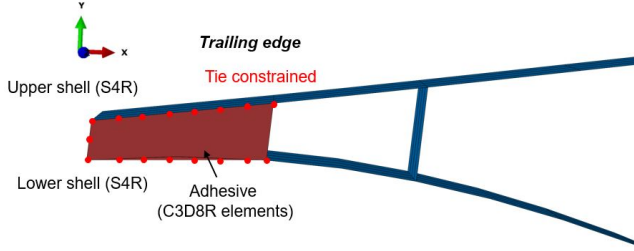


Figure 10: Modelling of adhesive joint at the trailing edge

from 0.5 mm - 4 mm throughout the length of the blade and the thickness of the adhesive at contact region 'A' is 1 mm. The modelling method also considers adhesive joints at the trailing edge. For this purpose, standard hexahedral continuum solid elements (C3D8R) are utilised for modelling the adhesive material and is tie-constrained with the aerodynamic shells at the trailing edge (fig. 10). The adhesive joints in the spar cap regions are modelled in a general manner with a simplified edge-to-edge joint. Additionally, the strength of the modelled blade based on conventional blade-type is found to be satisfactory in terms of global characteristics and is therefore suitable for impact analysis.

243 Blade tower impact formulation approach

244 A tower with a diameter of 5 m and a height of 120 m is defined as a rigid body in the analysis and
 245 is discretised with 4-node, bilinear quadrilateral (R3D4) elements (fig. 11). A reference point is allocated
 246 to the rigid tower along with an inertial mass of 450 tons, and it is fixed in all degrees of freedom.
 247 Furthermore, the blade is given an predefined impact velocity in the x -direction (V_x) ranging from 0.02
 248 m/s to 0.5 m/s. There was no other impact velocity defined in other directions (fig. 11). Further, no
 249 other elements used in the lifting of the blade, such as the yoke, crane hook or tugger lines, are modelled.
 250 The contact between the tower and blade is defined in the analysis based on a general contact formulation
 251 available in Abaqus and is defined between the shell reference surface and outer surface of the tower.
 252 The normal behaviour is defined as hard contact where as the tangential behaviour between the surfaces
 253 is defined with penalty algorithm and a value of 0.3 is defined as the friction coefficient. The entire
 254 blade is discretised with 4-noded quadrilateral shell elements (S4Rs) with a reduced integration scheme.
 255 The elements in the contact region of the blade for both blade-types have refined meshes with element
 256 dimension of $0.48 \times 0.48 \text{ m}^2$. Conversely, the remaining region of the blade, which contributes mainly to
 257 the inertia, is discretised with relatively coarser meshes with element size varying from 50 mm to 500 mm.
 258 This is based on a mesh convergence study performed in [4]. Overall, there were in total 97,356 elements
 259 present for both blade-types. Note that Abaqus/Explicit is the solver environment in this study because
 260 of its efficacy in solving highly non-linear problems with complex interactions, large rotations and large
 261 deformations.

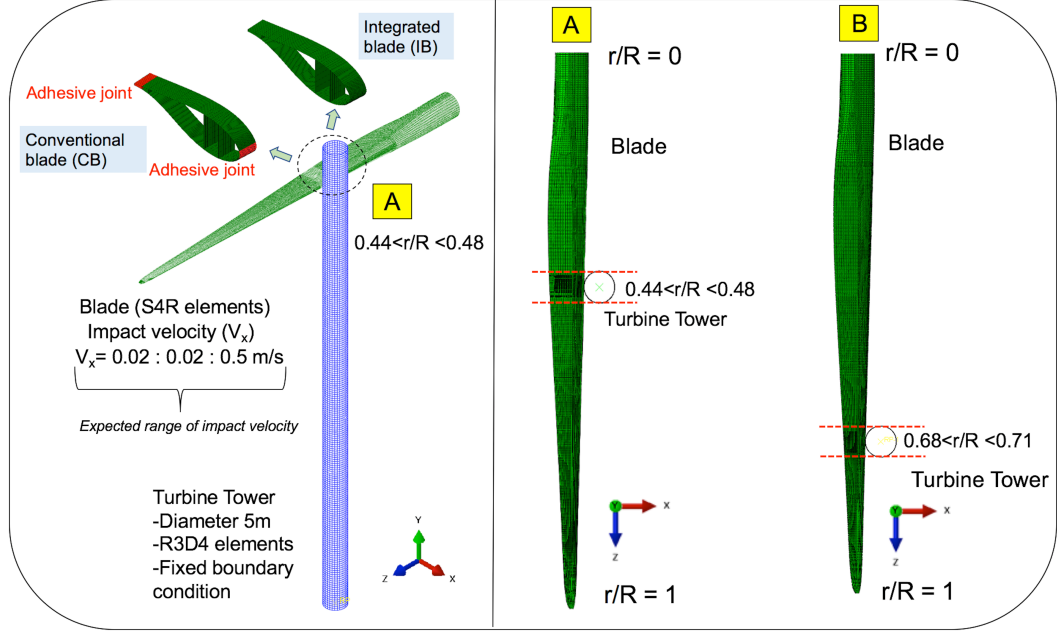


Figure 11: Details of numerical models considered in the paper

262 3. Constitutive material damage models implemented

263 This paper considers impact investigation for two distinct blade-type impacting the tower with their
 264 leading edge. Suitable damage models are thus required to model failure modes as different material
 265 combinations are present at the leading edge. These are explained below.

266 3.1. Progressive failure model for the composite ply

267 The 2D-Hashin failure criterion and the energy-based damage evolution law [27, 28, 29] are utilised
 268 for progressive modelling of damages in the composite ply. The damage initiation phase is determined
 269 by Hashin failure criterion and can be used to estimate fibre and matrix damage modes separately; it is
 270 given by the following:

271 1. Fibre tension ($\hat{\sigma}_{11} \geq 0$) :

$$F_{ft} = \left(\frac{\hat{\sigma}_{11}}{X^T} \right)^2 + \kappa \left(\frac{\hat{\tau}_{12}}{S^L} \right)^2 = 1 \quad (1)$$

272 2. Fibre compression ($\hat{\sigma}_{11} < 0$) :

$$F_{fc} = \left(\frac{\hat{\sigma}_{11}}{X^C} \right)^2 = 1 \quad (2)$$

273 3. Matrix tension ($\hat{\sigma}_{22} \geq 0$) :

$$F_{mt} = \left(\frac{\hat{\sigma}_{22}}{Y^T}\right)^2 + \left(\frac{\hat{\tau}_{12}}{S^L}\right)^2 = 1 \quad (3)$$

274 4. Matrix compression ($\hat{\sigma}_{22} < 0$) :

$$F_{mc} = \left(\frac{\hat{\sigma}_{22}}{2S^T}\right)^2 + [(\frac{Y^C}{2S^T})^2 - 1] \frac{\hat{\sigma}_{22}}{Y^C} + \left(\frac{\hat{\tau}_{12}}{S^L}\right)^2 = 1 \quad (4)$$

275 where in the above equations $\hat{\sigma}_{11}$, $\hat{\sigma}_{22}$ and $\hat{\tau}_{12}$ are effective stress tensor components of $\hat{\sigma}$ and utilized in
 276 the model to determine initiation of the different damage modes mentioned above. The effective stress
 277 tensor $\hat{\sigma}$ is derived from the true stress σ using the following relation:

$$\hat{\sigma} = M\sigma \quad (5)$$

278 where M is the matrix damage operator and is given by:

$$M = \begin{bmatrix} \frac{1}{(1-d_f)} & 0 & 0 \\ 0 & \frac{1}{(1-d_m)} & 0 \\ 0 & 0 & \frac{1}{(1-d_s)} \end{bmatrix} \quad (6)$$

279 where d_f , d_m and d_s are variables that characterise fibre, matrix, and shear damage and are derived from
 280 damage variables established based on the damage evolution laws in the respective failure modes (d_I and
 281 $I \in ft, fc, mt, mc$). The material parameters in the above equations X^T and X^C denote the longitudinal
 282 tensile and compressive strength respectively, Y^T and Y^C denote the transverse tensile and compressive
 283 strength respectively, and finally S^L and S^T denote the longitudinal and transverse shear strength of the
 284 ply, respectively. These material parameters are taken from [16, 20] and are mentioned in Table 2. κ in
 285 equation (1) defines the shear stress dependency to fibre tensile failure (F_{ft}) and is assumed to be zero in
 286 this work. Damage initiation in any respective ply is indicated when for a particular integration point F_{ft} ,
 287 F_{fc} , F_{mt} , or F_{mc} reach a value of unity. Once the damage initiation criterion is met, the evolution of the
 288 degradation of material stiffness and continuous update of damage variable in all 4 modes are determined
 289 by the evolution law. This evolution formulation is defined by a relation between stress and displacement
 290 together with linearised material softening and calculates the current damage state for the matrix and
 291 fibre. The damage variable will evolve in the manner represented in fig. 12 following a linear material
 292 softening behaviour. The negative slope from A to C will depend on $\delta^f eq$, which is as follows:

$$\delta^f eq = \frac{2G_{I,C}}{\sigma^0 eq} \quad (7)$$

293 where $G_{I,C}$ is the critical energy release rate corresponding to the area of triangle OAC and is defined for
 294 each damage mode. Moreover, based on this damage evolution law, the stiffness of the damaged element
 295 after the damage initiation point is evaluated using

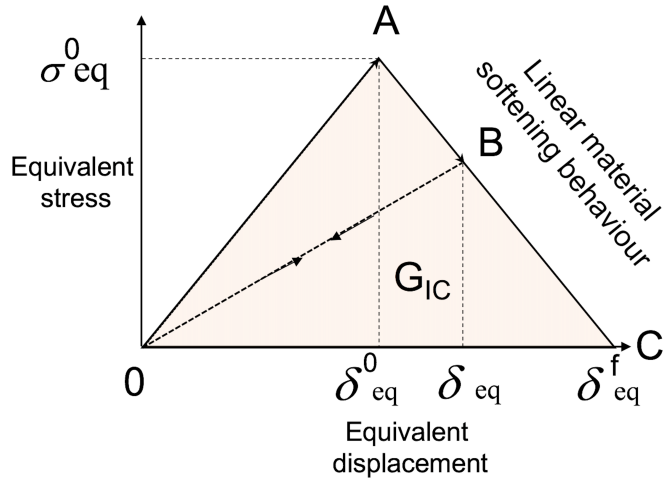


Figure 12: Equivalent stress versus equivalent displacement [25]

$$\sigma = C_d \epsilon \quad (8)$$

and C_d is the damaged material stiffness given by

$$C_d = \frac{1}{D} \begin{bmatrix} (1 - d_f)E_1 & (1 - d_f)(1 - d_m)\nu_{21}E_1 & 0 \\ (1 - d_f)(1 - d_m)\nu_{12}E_2 & (1 - d_m)E_2 & 0 \\ 0 & 0 & (1 - d_s)GD \end{bmatrix} \quad (9)$$

where

$$D = (1 - d_f)(1 - d_m)\nu_{21}\nu_{12} \quad (10)$$

$$d_f = \begin{cases} d_f^t, & \text{if, } \hat{\sigma}_{11} \geq 0 \\ d_f^c, & \text{if, } \hat{\sigma}_{11} < 0 \end{cases} \quad (11)$$

$$d_m = \begin{cases} d_m^t, & \text{if, } \hat{\sigma}_{22} \geq 0 \\ d_m^c, & \text{if, } \hat{\sigma}_{22} < 0 \end{cases} \quad (12)$$

$$d_s = (1 - d_f^t)(1 - d_f^c)(1 - d_m^t)(1 - d_m^c) \quad (13)$$

The parameters d_f , d_m , and d_s describe the final damage state of the ply in different modes corresponding to fibre and matrix failure in compression, tension and shear, respectively.

3.2. Failure criterion considered for the balsa core

A sandwich section consists of laminate face sheets and an added core in the middle. These sections are used because of the core's low density and aid in the local thickening of the section. This significantly

303 improves the buckling resistance of the section without any significant addition of extra weight. For
 304 estimating impact-induced damages on the leading edge of an integrated blade-type, balsa material in
 305 this study is considered as elastic-plastic and is defined to have isotropic hardening behaviour. The failure
 306 criterion is defined by von Mises yield stress formulation together with equivalent plastic strain measure.
 307 This criterion is simple and has been utilised in the literature [30, 31] for modeling the inelastic behaviour
 308 of balsa core material during impact on a sandwich section. However, it should be noted that the balsa is
 309 an anisotropic material, and a more detailed criterion that includes hydrostatic dependency, strain rate
 310 effects and anisotropicity must be considered. Currently, there are no built-in criteria implemented in
 311 Abaqus for modelling impact on balsa for shell-element-based formulations, and therefore, in this study,
 312 a simplified criterion based on von Mises is used. Note that the shell element kinematics do not have a
 313 constitutive relation for the displacements in the thickness direction and therefore cannot capture crushing
 314 and inelastic deformation in the thickness direction of the core. However, the applied criterion enables the
 315 model to capture inelastic deformation at least in the in-plane loading directions of the core. Furthermore,
 316 the impact velocities in the paper lie within the low-velocity impact regime, and therefore, the chosen
 317 failure criterion is considered suitable for modelling impact-induced damages. The material parameters
 318 for the balsa material are taken from previous studies [30, 31, 32] and are listed in Table 2.

319 3.3. Material damage model considered for the adhesive

320 There has been a record of various failure criteria utilised for adhesives in the past, but there is no
 321 single and unique failure criterion applicable for all cases [33, 34]. Yield-based failure criteria such as von
 322 Mises assume yielding to be a pure shear deformation failure and neglect hydrostatic stresses. Therefore,
 323 such criteria are not suited to model adhesives [34], given that these materials are sensitive to both
 324 hydrostatic stress and shear components. The exponential-based Drucker Prager yield criterion, which is
 325 an extension of the von Mises yield criterion [33, 35], considers the sensitivity of adhesives to hydrostatic
 326 stresses and is found to be a sound criterion to model failure in adhesives; thus, it is utilised in the study.
 327 The adhesive used in the conventional blade-type in the paper is Araldite 2015 [36], which is a ductile
 328 adhesive from Huntsman. The material data for the adhesive are derived from [35] and are listed in Table
 329 3. A very brief explanation of the exponential-based Drucker-Prager model is provided below. Note that
 330 the data corresponding to true plastic stress-plastic strain under tensile uniaxial directions are used in
 331 the model along with tensile-type hardening behaviour. The yielding in the adhesives is considered with
 332 isotropic hardening. A general yield function of the exponential-based Drucker-Prager model is based on
 333 the following [fig. 13]:

$$F = aq^b - p - p_t \quad (14)$$

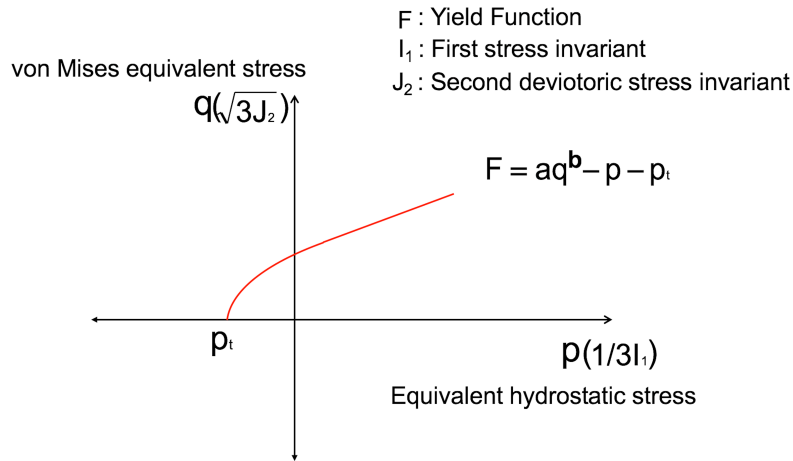


Figure 13: Yield surface of Exponent Drucker-Prager model in meridian plane

Table 2: Material properties implemented in this study [20]

Property	GFRP	Balsa	Units
Density (ρ)	1915.5	110	Kg/m ³
E_1	41.63	0.050	GPa
E_2	14.93	0.050	GPa
E_3	13.42	2.730	GPa
G_{12}	5.047	0.0167	GPa
$G_{23} = G_{13}$	5.0469	0.150	GPa
ν_{12}	0.241	0.5	-
ν_{13}	0.2675	0.013	-
ν_{23}	0.33	0.013	-
X_T	903.6	-	MPa
X_C	660.1	-	MPa
$Y_T = Y_C$	42.1	-	MPa
$S_L = S_T$	58.65	-	MPa

334 where p_t is defined as the hardening parameters that corresponds to the hydrostatic tension strength of
 335 the adhesive and are derived based on different uniaxial tests on adhesives, q is the equivalent stress, and p
 336 is the hydrostatic stress. Here, b is called the exponent parameter and was taken to have a standard value
 337 of 2 based on [30]. Additionally, a is a material parameter constant with respect to stress (considering

Table 3: Material properties implemented for adhesive [35]

Property	Adhesive	Units
Density (ρ)	1400	Kg/m ³
E	1850	MPa
G	560	MPa
ν	0.33	-
σ_y	13.3	MPa
σ_t	21.63	MPa
m	1.4	-
a	0.041	-
b	2	-
Dilation angle	13 ⁰	-

338 isotropic hardening) and independent of plastic deformations that is given by

$$a = \frac{1}{3(\sigma_{yc} - \sigma_{yt})} = \frac{1}{3(m-1)\sigma_{yt}}; m = \frac{\sigma_{yc}}{\sigma_{yt}} \quad (15)$$

339 where 'm' is the hydrostatic sensitive parameter of the adhesive and σ_{yt} and σ_{yc} are the tensile yield
340 stress and compressive yield stress of the adhesive.

341 4. Results and discussion

342 The results regarding the impact dynamics, energy evolution history and damage assessment for the
343 case in which the wind turbine blade impacts the tower with its leading edge are presented here. The
344 impact investigations are performed for two distinct blade types (integrated blade-type and conventional
345 blade-type), two impact locations (contact regions A and B) and different impact velocities in the range of
346 0.02 m/s to 0.5 m/s. An individual explanation for all the cases is not possible, and thus, the results are
347 presented for important cases. Table 4 presents a summary of various cases considered in this section for
348 discussion along with major results. Case I compares the results regarding impact dynamics for varying
349 impact location (contact regions A and B), and the discussion is restricted to the integrated blade-type and
350 impact velocity of 0.08 m/s. For the purpose of discussing the energy evolution and damage assessment
351 results, both the conventional blade-type and integrated blade-type are utilised. However, only impacts at
352 contact region A are considered. These are discussed through Case II, Case III and Case V. Finally, Case

Table 4: Summary of cases considered for discussion along with major results

Blade-type	Case name	Contact region	Velocity of impact V_x (m/s)	Major results discussed
A. Integrated blade-type	Case I	A	0.08	Impact dynamics Energy evolution history Damage Assessment
	Case I	B	0.08	Impact dynamics Energy evolution history Damage Assessment
	Case II	A	0.15	Energy evolution history Damage Assessment
	Case III	A	0.5	Energy evolution history Damage Assessment
	Case IV	A	[0.02,0.5]	Relationship DE and V_x DE ratio with total energy (TE)
B. Conventional blade-type	Case V	A	0.5	Energy evolution history Damage Assessment Compare with 'A' type blade
	Case VI	A	[0.02,0.5]	Relationship DE and V_x DE ratio with total energy (TE)

353 IV and Case VI present the results for all cases of impact velocities, and an analytical relation between
 354 the damage energy (DE) and velocity of impact (V_x) is established for both blade-types.

355 *4.1. Description of impact dynamics*

356 *Case I. Velocity of impact $V_x=0.08$ m/s, Contact Regions A and B*

357 The impact dynamics, including the energy evolution history and motion of the blade after the impact,
 358 will be discussed here for the case in which the blade impacts the tower with its leading edge. Two different
 359 contact regions, i.e., regions A and B, are considered. Here, an impact velocity of 0.08 m/s is used for the
 360 discussion because no damages developed in the blade for this case, and it was thus suitable to explain
 361 and compare the impact dynamics.

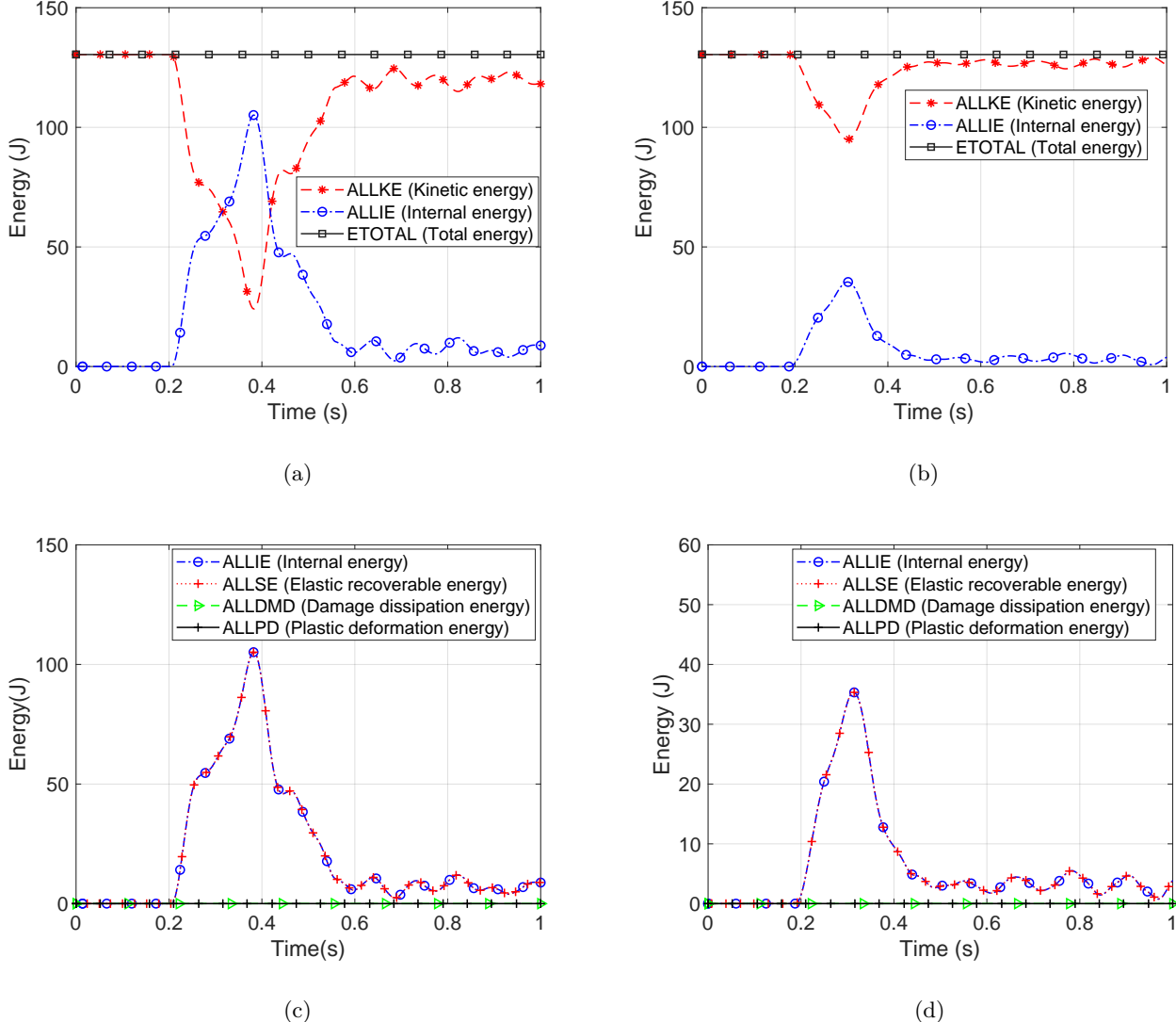


Figure 14: (a) Evolution of ALLKE, ALLIE, ETOTAL (Contact Region A), $V_x=0.08$ m/s (b) Evolution of ALLKE, ALLIE, ETOTAL (Contact Region B), $V_x=0.08$ m/s (c) Dissipation of internal energy (ALLIE) (Contact Region A) (d) Dissipation of internal energy (ALLIE) (Contact Region B)

362 *Energy evolution history:*

363 One of the important results for impact dynamics based on an explicit solver based analysis is the
 364 validation of the energy conservation principle. Figs. 14 (a) and 14 (b) present the evolution of kinetic
 365 energy, internal energy and total energy for the case of a blade impacting the tower with contact region A
 366 and B respectively. It can be observed that the total energy (ETOTAL) of the system in the simulation
 367 is constant. Also, at any time step of the simulation, the total energy (ETOTAL) corresponds to the sum
 368 of internal energy (ALLIE) and kinetic energy (ALLKE). This confirms the theory of energy conservation
 369 balance in the system for both the contact regions. Further, it is also checked that the artificial energy

370 developed during the simulation corresponds to less than 2% of the total energy. Therefore, the numerical
371 model is considered suitable and gives stable results.

372 From figs. 14(a) and (b), it can also be seen that for both the cases, the blade comes into contact
373 with the tower at a simulation time of approximately 0.2 s. Additionally as the impact occurs, the
374 internal energy (ALLIE) is developed in the blade with corresponding decline in the level of kinetic
375 energy (ALLKE). Note that the ALLIE developed due to impact is utilised in general as recoverable
376 strain energy (ALLSE), damage dissipation energy (ALLDMD) and energy dissipated due to plastic
377 deformation (ALLPD) in the system. Figs. 14 (c) and 14 (d) present the evolution of total internal
378 energy (ALLIE) and its dissipation into ALLSE, ALLPD and ALLDMD for both the contact regions A
379 and B respectively. It can be seen that ALLIE and ALLSE are similar through out the simulation time
380 and thus completely overlap each other. Further, there is no development of ALLDMD and ALLPD in
381 the blade. This implies that for both the case of impact with contact region A and B, there is no damage
382 developed in the blade at an impact velocity of 0.08 m/s. Hence, all the developed internal energy (ALLIE)
383 dissipates as recoverable elastic strain energy (ALLSE). Note that this a qualitative indication of having
384 no damage in the blade based on energy results. A quantitative description is also discussed later where
385 the damage assessment results are presented.

386 *Kinematics of the lifted blade after the impact:*

387 The energy evolution histories for the case in which the blade impacts the tower at contact regions A
388 and B for $V_x = 0.08$ m/s were discussed based on figs. 14(a) and 14 (b). It is seen that the ETOTAL (135
389 J) for both the cases are identical given that they correspond to same impact speed (0.08 m/s). However,
390 there is a significant difference in the natures of the evolution of ALLKE and ALLIE for contact regions
391 A and B; see figs. 14 (a) and 14 (b). For the case in which the blade impacts the tower at contact region
392 B, there is less dissipation of ALLKE and ALLIE, compared to impact of the blade at contact region A.
393 Further, for contact region B, the impact of the blade with the tower persists for a small contact duration
394 (0.2 s-0.39 s) compared to the contact duration of (0.2 s-0.59 s) for impact at contact region A.

395 The argument is also confirmed from fig. 15, where the contact-force time histories are compared for
396 contact regions A and B. It is seen that for contact region B, the contact duration and contact forces are
397 less compared to the blade impacting the tower at contact region A.

398 The reason for the difference in the impact dynamics for the two cases is the eccentricity at the location
399 of impact. The impact at contact region B represents a highly eccentric impact ($e=34$ m) compared to
400 contact region A, which is close to the COG ($e=11$ m), see figs. 16 and 17. Moreover, the section of
401 the blade at contact region B is lighter in mass, is narrower and has a relatively smaller chord length of
402 approximately 3.46 m. Therefore, once the blade impacts the tower at contact region B, as a result of

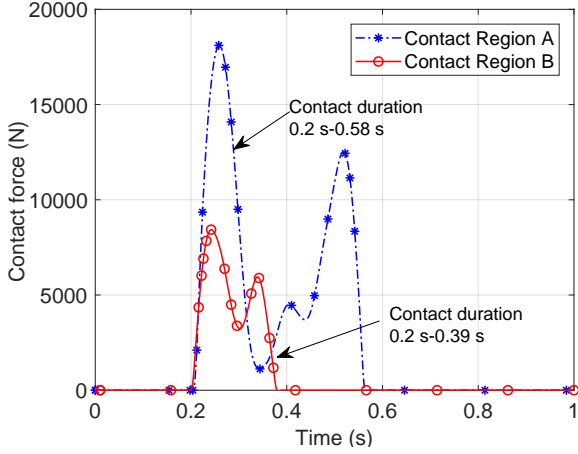


Figure 15: Contact-force history comparison (Contact region A and B), $V_x=0.08 \text{ m/s}$

the eccentricity and difference in mass distributions, an unbalanced moment is created at the blade root side. Thus, the blade starts to deflect and rebound even before the whole contact/impact with the tower completes. As a result, not much kinetic energy (ALLKE) is transformed into internal energy (ALLIE) and a small contact duration is seen.

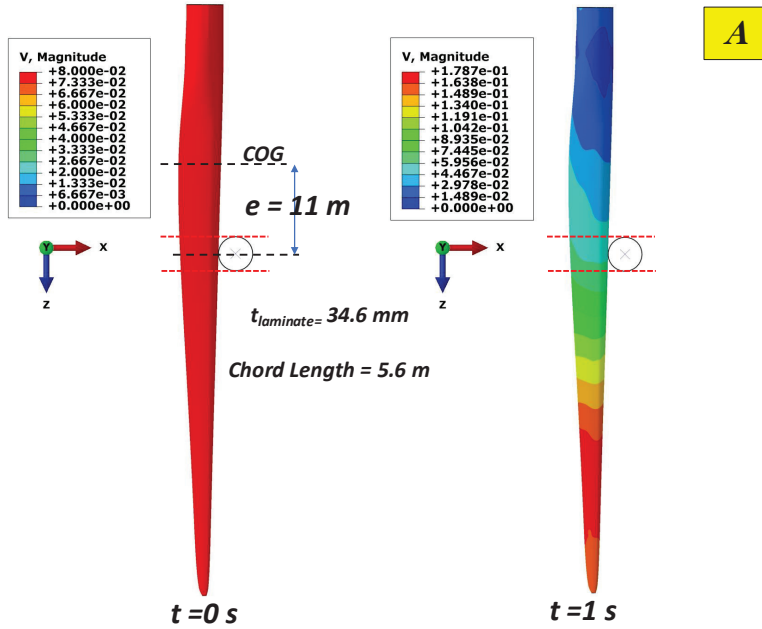


Figure 16: Velocity contour after impact (Contact Region A)

A significant difference in the motion of the blade after the impact for the two cases can also be observed from figs. 16 and 17. For contact region B, the velocity is dominant both at blade root and in the tip region (fig. 17) and thus a significant rotation of the blade after the impact is observed. However, for the impact of blade at contact region A, the velocity and the motion of the blade is concentrated

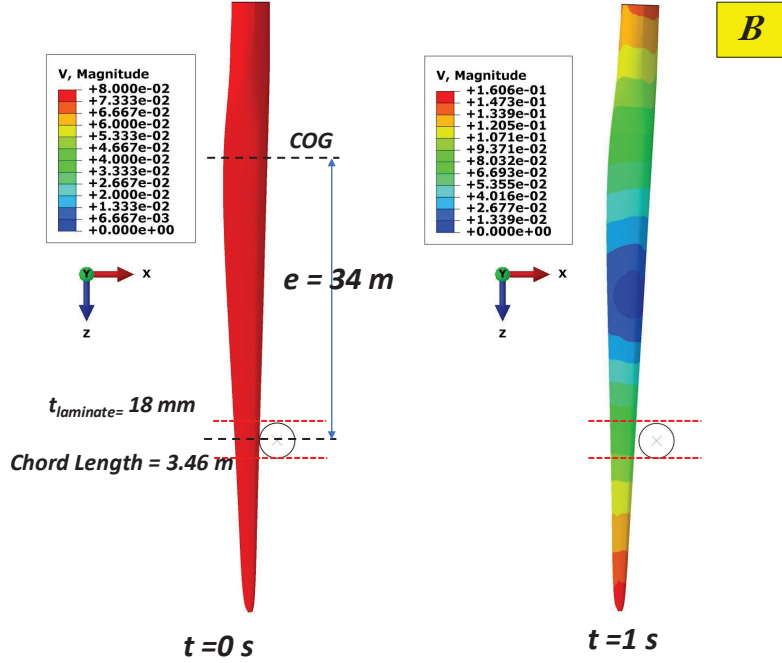


Figure 17: Velocity contour after impact (Contact Region B)

411 explicitly at the tip region (fig. 16). It is also worth mentioning that for the case of blade impacting the
 412 tower at contact region A, there are vibrations present in the blade after the impact. However, for the
 413 case of blade impacting the tower at contact region B, there are more rigid-body rotational motions of the
 414 blade and less vibrations. This is an important observation because the control forces for active tugger
 415 lines would be required to dampen these vibrations in the blade if the impact occurs closer to the yoke.

416 *Quantified description of damage based on the damage model:*

417 In the current discussion based on energy evolution, it is qualitatively argued that there are no damages
 418 developed in the blade due to impact. A quantified description based on the damage model is presented
 419 here. Figs. 18 (a) and 18 (b) present the ply-wise Hashin failure initiation criterion state for impact
 420 regions A and B and impact velocity of 0.08 m/s. It can be observed that none of the plies at these
 421 regions had Hashin failure initiation criteria equal to one. This implies that no damage is initiated in the
 422 blade at $V_x = 0.08$ m/s. Further, the von Mises stresses in the balsa layer are below the yield stresses,
 423 and this result confirms that no plastic strain are induced in the blade either. These results also confirms
 424 the energy evolution results in which no ALLDMD or ALLPD are reported; see fig. 14(b). Overall, no
 425 damage develops in the blade for this case and thus $V_x = 0.08$ m/s lies below the threshold velocity at
 426 which damage initiates.

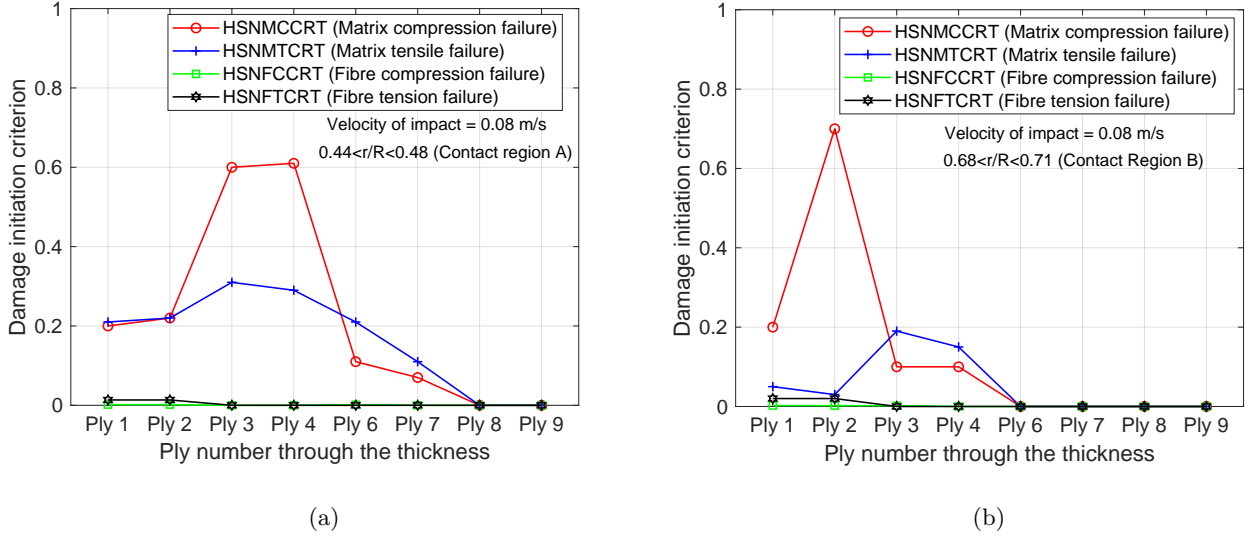


Figure 18: Ply-wise damage initiation criterion, $V_x=0.08$ m/s (a) contact region A (b) contact region B

427 4.2. Impact-induced damage assessment for integrated and conventional blade-types

428 In this section, damage assessment results in the blade for higher impact velocities are presented. The
 429 focus of the discussion is explicitly on the nature of damages obtained for both the blade-types. Hence,
 430 the results are restricted for the case of blade impacting the tower at contact region A. The paper first
 431 discusses the damage assessment results for integrated blade-type (through Case II, III and IV), followed
 432 by a discussion of the conventional blade-type (through Case V and VI) in the next section.

433 A. Integrated blade-type

434 Case II. Velocity of impact $V_x=0.15$ m/s

435 In the previous section, for the case of a blade impacting the tower with $V_x = 0.08$ m/s, it is found that
 436 there are no impact-induced damage developed in the blade. All the internal energy (ALLIE) developed
 437 due to impact dissipates as recoverable elastic strain energy (ALLSE). Here, the damage assessment result
 438 is presented for $V_x = 0.15$ m/s, which corresponds to approximately 450 J of impact energy. Note that
 439 the impact energy considered is about 3.2 times compared to the case of $V_x = 0.08$ m/s. Fig. 19 (a)
 440 presents the energy evolution history for ALLIE, ALLKE and ETOTAL. It is observed that the total
 441 energy of the system remains steady throughout the simulation time, and ALLKE and ALLIE correspond
 442 to ETOTAL. This confirms the theory of energy conservation principle. Also seen from the figures, the
 443 blade impacts the tower at a simulation time of approximately 0.16 s, and at this moment, the internal
 444 energy in the blade originates with a corresponding decrease in the kinetic energy (ALLKE). However,
 445 unlike for the case of $V_x = 0.08$ m/s, ALLIE and ALLSE are no longer similar throughout the simulation
 446 time and do not overlap. It is seen from fig. 19 (b) that ALLIE and ALLSE only overlap until a simulation

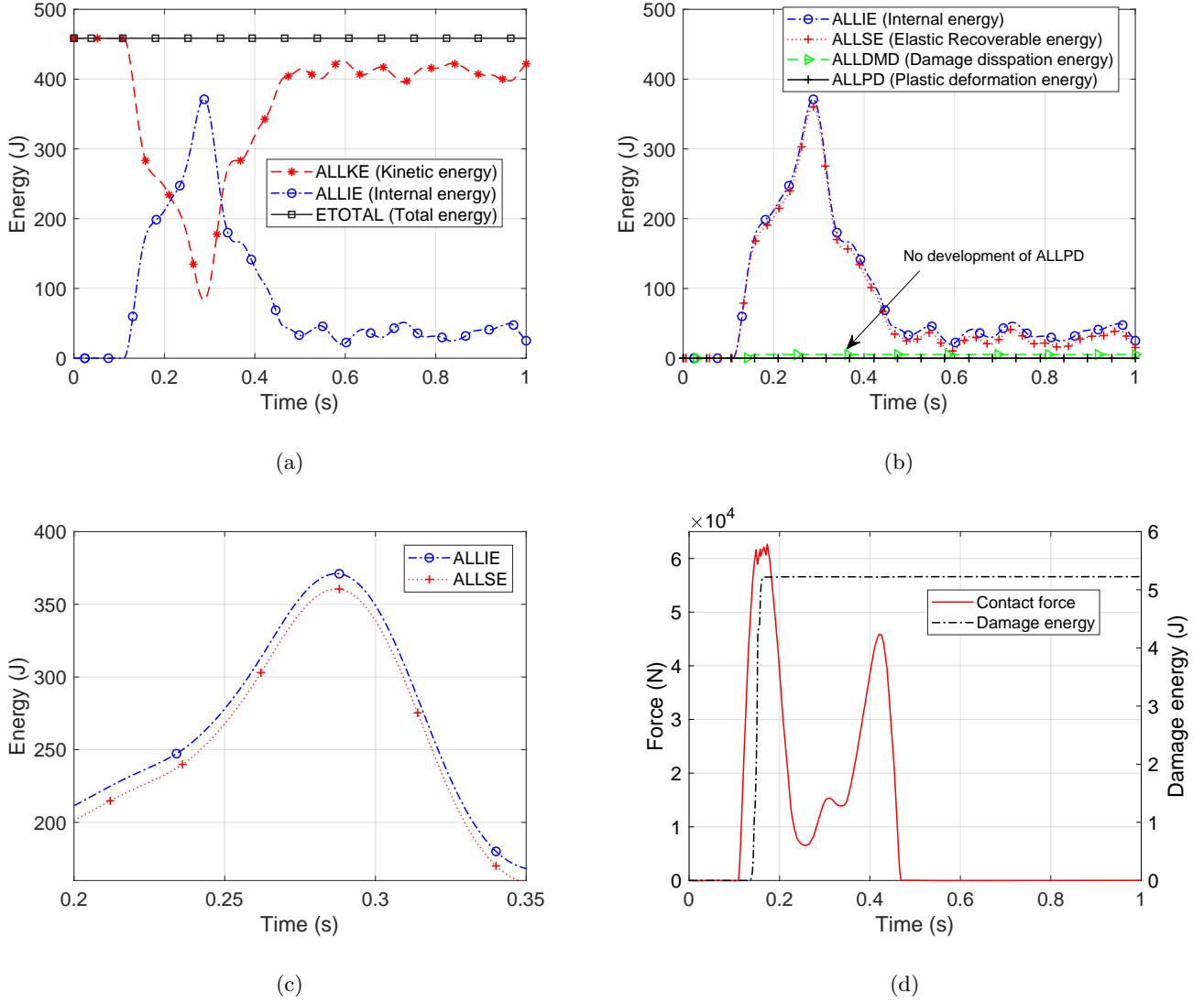


Figure 19: (a) Evolution of ALLKE, ALLIE, ETOTAL ($V_x = 0.15$ m/s) (b) Dissipation of internal energy (ALLIE), ($V_x = 0.15$ m/s) (c) Difference in the level of ALLIE and ALLSE (d) Contact force comparison with the ALLDMD, ($V_x = 0.15$ m/s)

time of 0.18s, followed by a small difference in the level of ALLIE and ALLSE afterwards. This result can be further confirmed from fig. 19 (c) where the evolution of ALLIE and ALLSE for 0.2 s - 0.35 s is magnified and presented. Note that this difference between ALLIE and ALLSE is utilised in the blade as the damage energy (ALLDMD), which is also seen in fig. 19 (b). This result implies that for the case of the blade impacting the tower with $V_x = 0.15$ m/s, not all the internal energy (ALLIE) developed in the blade is dissipated as recoverable elastic strain energy (ALLSE); and this indicates damage development in the blade given by ALLDMD.

Fig. 19(d) presents a comparison of contact force history with the damage energy developed in the blade. It can be seen that the damage energy (ALLDMD) follows the curve of the contact force history,

456 with maximum damage energy accumulated at the point at which there is the largest contact force. Note
 457 that at the point at which ALLDMD appears, the contact force curve (at the first peak) exhibits an
 458 oscillating nature with a change in the slope. This indicates a change in the material stiffness and damage
 459 progression in the blade.

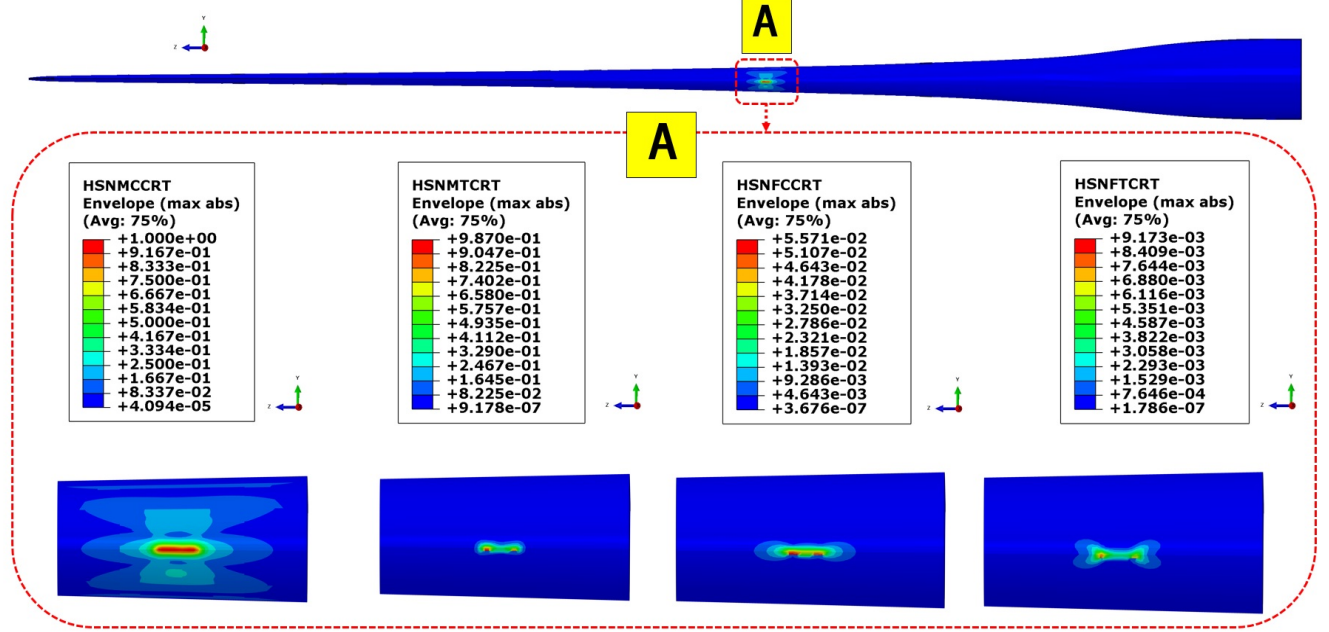


Figure 20: Damage initiation status based on Hashin failure criterion, Contact region A (Integrated blade-type, $V_x=0.15$ m/s)

460 A quantified description of damage assessment is presented in fig. 20 in which the damage state of
 461 the blade based on Hashin's failure initiation criterion is illustrated. It can be observed that the status
 462 HSNMCCRT has reached a value 1, which means that the damage initiation criterion has been met and
 463 the laminate has initiated damage in matrix compression. The damage status HSNMTCRT, HSNFCCRT,
 464 HSNFTCRT are less than 1 indicating no damage in other failure modes. This discussion is in line with
 465 the small damage energy (ALLDMD) dissipated due to impact and thus indicates a minor damage in the
 466 blade. It is also found that the von Mises stresses in the core are less than the yield stresses and thus no
 467 damage initiation or inelastic deformation is developed in the core. This compliments the energy results
 468 where no ALLPD are reported due to impact, see fig. 19 (b). Overall, minor damages are developed in
 469 the laminates for this case and thus $V_x = 0.15$ m/s lies just above the threshold velocity at which damage
 470 starts to initiate. Fig. 21 presents the maximum damage energy obtained in the blade due to impact for
 471 various impact velocities upto $V_x = 0.16$ m/s. It is seen that until $V_x = 0.14$ m/s, there is no development
 472 of damage energy; the development of damage energy initiates at 0.14 m/s. This implies that $V_x = 0.14$
 473 m/s is the threshold velocity of impact at which damage initiates in the blade. Note that these values

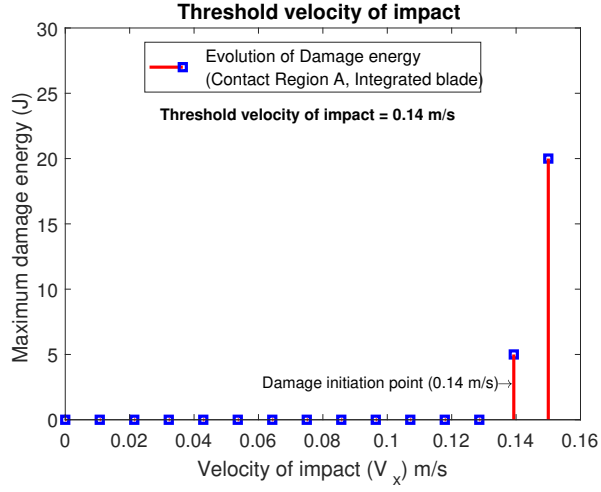


Figure 21: Determination of threshold velocity of impact

474 are sensitive to the layup plan and would vary with the specifics of the blade utilised in actual practice.
 475 Here, the paper presents these results for impact investigations based on the reference DTU blade and
 476 considers the integrated type of blade design. Note that these parameters aid in deriving response-based
 477 operational limits and is well captured through shell-element-based method.

478 ***Case III. Velocity of impact $V_x = 0.5 \text{ m/s}$***

479 In the previous cases, ply-level description of the damage in the blade was not mentioned because
 480 the damage obtained was minor. Here, the damage assessment result is presented for $V_x = 0.5 \text{ m/s}$,
 481 which corresponds to an impact energy of greater than 5000 J, and the final damage states in the blade
 482 is presented at the ply level.

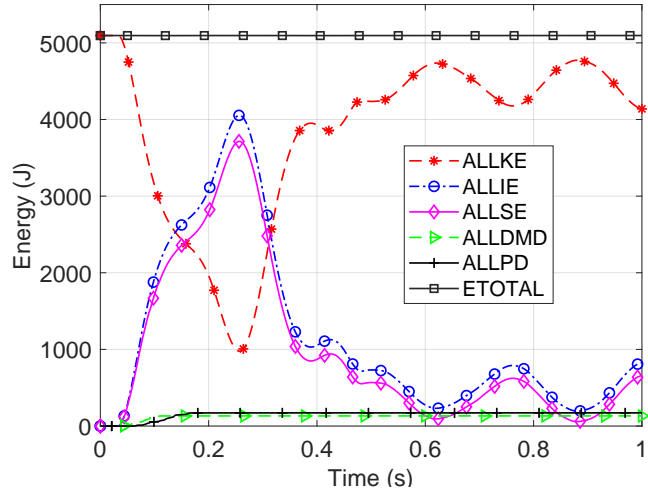


Figure 22: Evolution of various energies, ($V_x=0.5 \text{ m/s}$)

Fig. 22 shows the energy evolution history due to blade impact with the tower for $V_x=0.5$ m/s. The blade contacts the tower at a simulation time of approximately 0.05 s, and at this point, the internal energy (ALLIE) is developed in the blade and ALLKE decreases. Furthermore, the energy conservation principle can also be confirmed because the ETOTAL in the system is constant throughout the analysis and ALLKE and ALLIE correspond to ETOTAL at every time step. Fig. 22 also presents the dissipation of developed ALLIE into corresponding ALLSE, ALLDMD and ALLPD. It can be seen that there is a large difference in the curves of ALLIE and ALLSE, and a significant development of damage dissipation energy (ALLDMD) and plastic deformation energy (ALLPD). This indicates large damages and degradation of material stiffness at the contact region. The development of ALLPD in the energy curves also qualitatively indicates the development of inelastic deformation in the core. A quantitative description of the damage states of the blade's leading edge due to impact for this case is presented below.

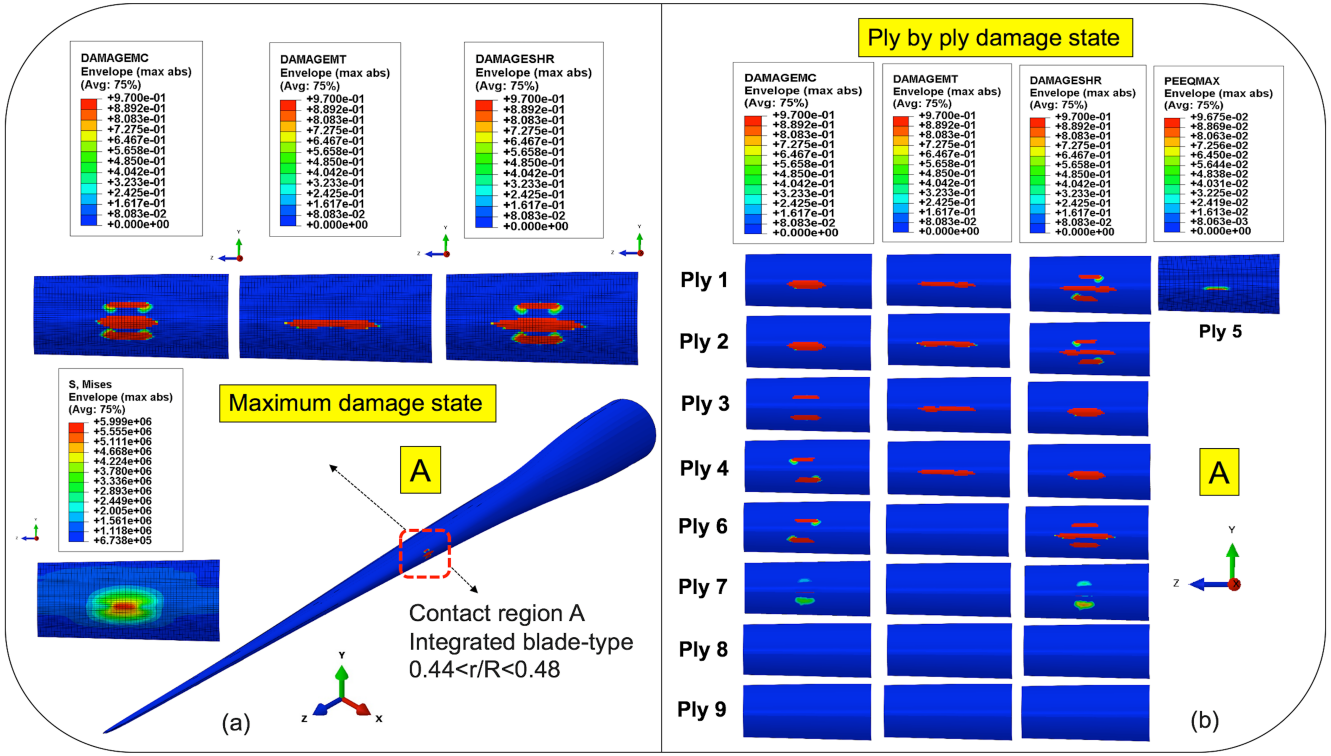


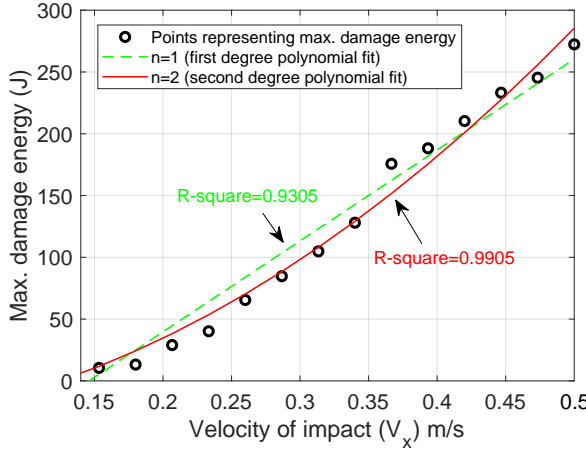
Figure 23: Damage state for the contact region A at $t=1$ s (Integrated blade-type, $V_x=0.5$ m/s)

Fig. 23 shows the final damage state of the blade due to impact with the tower at the simulation time $t=1$ s. Fig. 23 (a) illustrates the envelope view of the damage states. It can be clearly seen that the blade has developed damage in matrix compression (DAMAGEMC), matrix tension (DAMAGEMT) and shear (DAMAGESHR). This result implies that the blade damage due to impact are matrix-dominated. Furthermore, the von Mises stresses in the core (5.99 MPa) exceed the yield strength (5.4 MPa), which indicates the development of plastic strain and inelastic deformation. The discussion is also elaborated at

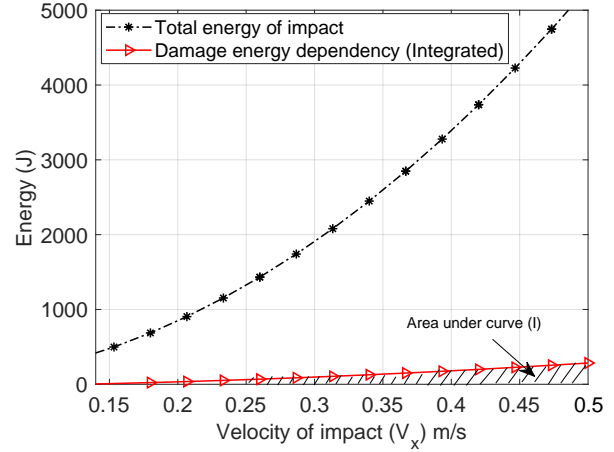
the ply scale in fig. 23(b), in which the damage states for various plies in the contact region are presented. Note that the results are presented for the middlemost section point of each ply. It can be observed from the figure that most of the plies exhibited damage near the impact side of the laminate (i.e., between plies 1 and 4), with damage further developing in the plies below the core. Moreover, different plies had different regions being damaged, which is due to the plies' varying orientations and the presence of curvature in the impact region. Ply 5 corresponds to the balsa material, and the plastic strain (PEEQ) is also shown in fig. 23 (b). The discussion is in line with the energy evolution history, in which the development of ALLPD was reported; see fig. 22. Overall, it is seen that the intralaminar failure modes for the ply and damage state of the balsa is modelled at a ply level based on the modelling technique presented in this paper. However, one of the most important failure modes, which is delamination developing at the ply interfaces, are not modelled. The research task of modelling delamination in the blade due to impact can be achieved using a suitable global-local methods and will be considered in future work. However, the results obtained for the blade based on shell elements are important and will be utilised.

Case IV. Dependence of the damage energy (DE) on the impact velocity (V_x):

In the previous section, the damage assessment results for the integrated blade-type were presented for two impact velocities: 0.15 m/s and 0.5 m/s. Note that the impact investigations are performed for different velocities ranging from 0.02 m/s- 0.5 m/s. It was mentioned in section 1 that a dependency of damage energy (DE) on the impact velocity (V_x) is required to derive structural response-based operational limits. Fig. 24 (a) presents the maximum damage energies (ALLDMD) obtained in the blade for different impact velocities ranging from 0.14 m/s to 0.5 m/s (post-threshold range), which are represented by black dots. To establish an analytical relation between damage energies and different impact velocities, these points were fitted using first-order and second-order polynomial fits, which are represented by green and red lines, respectively; see fig. 24 (a). It can be observed that these points are represented better by the second-degree polynomial fit (red line, R-square=0.995), and thus, the relation ($DE = 735.72V_x^2 + 107V_x$) is found to be suitable to describe the dependence of the damage energy (DE) on the impact velocity (V_x). Furthermore, this dependence of the damage energy ($DE = 735.72V_x^2 + 107V_x$) is plotted and compared with the line representing the total energy of impact for all the cases ($KE = 0.5 \times \text{mass of the blade} \times V_x^2$); see fig. 24 (b). It can be seen that the area under the curve (I) for the damage energy line is considerably smaller than the total energy of impact. This result implies that a very small amount of impact energy (approximately 2-5%) is dissipated in the blade as damage, and most of the energy is dissipated as recoverable elastic strain energy by means of rigid-body motions and rotation of the blade after the impact. Thus, it is important to realise that the blade, when it impacts the tower while being lifted, dissipates only a small fraction of energy as damage, and the majority dissipates as recoverable



(a)



(b)

Figure 24: (a) Damage energy polynomial curve fitting (b) Comparison of damage energy with total energy of impact

533 elastic energy.

534 **B. Conventional blade-type**

535 The previous section described the damage assessment results for the case in which the blade modelled
 536 based on integrated blade-type impacts the tower with its leading edge. In this section, the results for
 537 damage assessment for conventional blade-type will be discussed. The focus is on the comparing the results
 538 with the integrated blade-type and thus impact velocity of 0.5 m/s (Case V) is explicitly considered. This
 539 is because for $V_x = 0.5$ m/s, significant damages are obtained in the previous discussions and is thus
 540 suitable for comparison. Finally, dependence of damage energy (DE) on the impact velocity (V_x) is
 541 presented for conventional blade-type (Case VI) and is compared with integrated blade-type.

542 **Case V. Velocity of impact $V_x = 0.5$ m/s**

543 Fig. 25 (a) presents the energy evolution history for ALLKE, ALLIE and ETOTAL for the case in
 544 which a conventional blade-type impacts the tower with $V_x = 0.5$ m/s. The total energy of the system is
 545 constant throughout the analysis, and ALLIE and ALLKE corresponds to ETOTAL at each time step of
 546 the simulation. Thus, the energy conservation principle is satisfied and the model is suitable for impact
 547 investigation. It can also be seen from the figure that the blade impacts the tower at around 0.05 s
 548 of the simulation time, and the internal energy (ALLIE) is developed at this point. The contact with
 549 the tower persists till 0.6 s, and the blade rebounds. Fig. 25 (b) presents the dissipation of internal
 550 energy into ALLSE, ALLDMD and ALLPD. It can be seen that there is large difference between ALLIE
 551 and ALLSE, which is about 5 times compared to integrated blade-type. Similarly, large damage energy
 552 (ALLDMD) in the blade is developed. This observation indicates that the there will be greater damage to

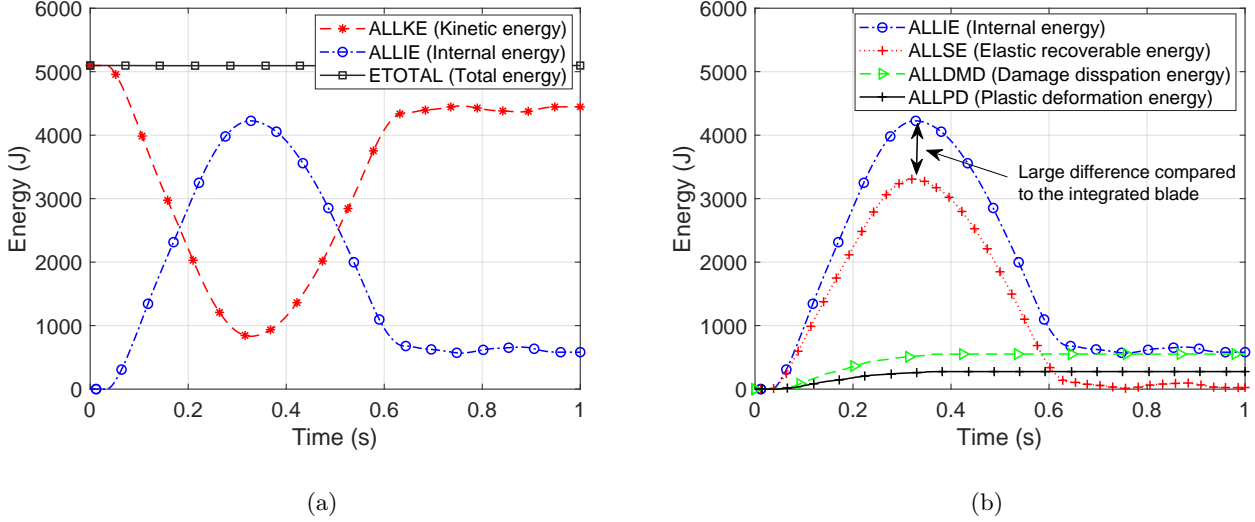


Figure 25: (a) Evolution of ALLKE, ALLIE, ETOTAL ($V_x = 0.5$ m/s) (b) Dissipation of internal energy (ALLIE), ($V_x = 0.5$ m/s)

a conventional-type blade than to an integrated-type blade. A quantitative description is also presented in fig. 26 where an envelope view of the damage state is shown. The conventional blade-type at the impact region has greater damages over large area based on DAMAGEMC, DAMAGEMT and DAMAGESHR status compared to integrated blade-type for the same impact velocity. The damage state through the thickness in corresponding DAMAGEMC, DAMAGEMT and DAMAGESHR is also presented in Fig. 27. It can be clearly observed that all the plies through the thickness developed a significant damage state. This observation is contradictory to what was obtained for integrated blade-type, where most of the damages were concentrated at the topmost plies and near the impact side. Fig. 25 (b) also presents the development of ALLPD which indicates the development of plastic strain in the blade at the contact region. This is confirmed quantitatively in Fig. 26, in which the plastic strain developed in the adhesive region due to the impact is shown. Note that the level of plastic strain developed is comparatively less than what was obtained for the layer of balsa for the integrated blade-type.

The reason for the difference in the damage resistance for both the blade-type is the nature and the thickness of the material present in the impact region. The integrated blade-type is fused with balsa material at the leading edge and has a thicker section (34 mm). Therefore, due to impact with the tower, much of the internal energy developed in the blade was absorbed by the thicker balsa layer, and not much damage developed below the core. As a result, most of the damages was focused around the impact side of the blade along the top plies, and less ALLDMD and a small damage area developed. On the other hand, the conventional blade-type was modelled with adhesive joint at the leading edge. The impact region for this blade was relatively thinner (10.2 mm) and therefore, for the same impact speed, most of

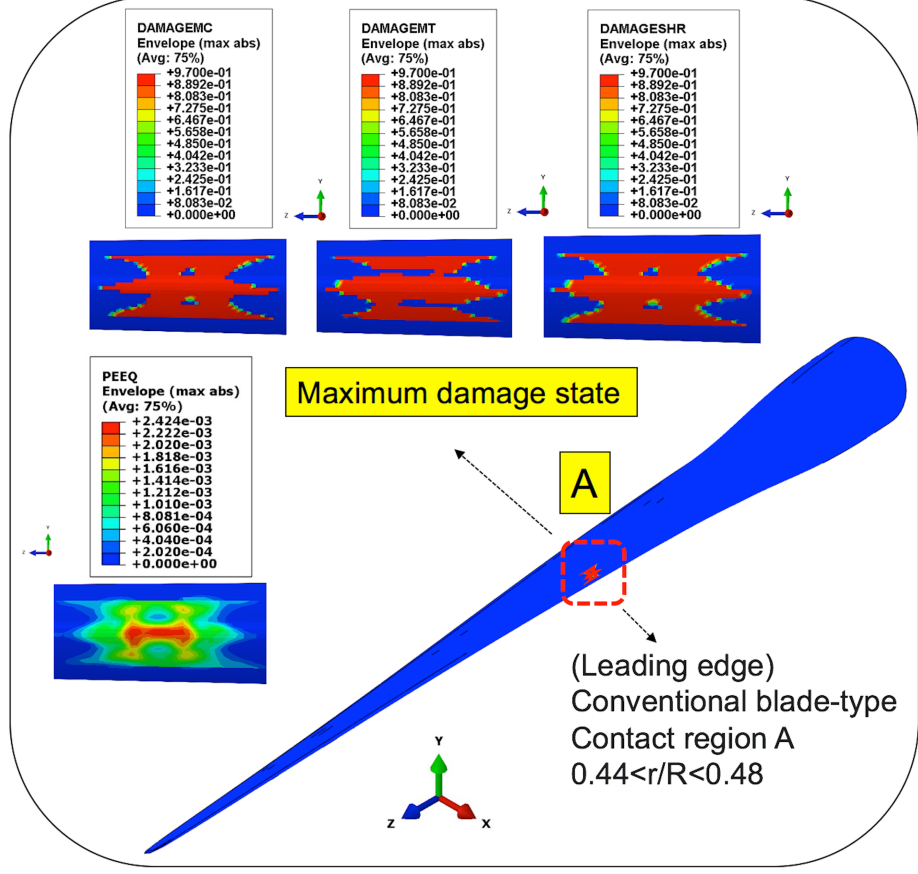


Figure 26: Damage state of the conventional blade-type, ($V_x = 0.5$ m/s)

573 the energy progressed to all the layers with damage spreading over larger area in the plies.

574 ***Case VI. Dependence of damage energy (DE) on the impact velocity (V_x):***

575 Previously, the dependence of damage energy (DE) on the impact velocity (V_x) was established
 576 and presented for integrated blade-type. Here, this dependency is compared with the results based
 577 on conventional blade-type. Fig. 28 presents the dependence of damage energy for the conventional
 578 blade-type on the impact velocity. As expected, the damage energy curve exhibits a stronger trend for
 579 conventional blade-type compared to the integrated blade type. This is due to the large damage energy
 580 (ALLDMD) developed in the case of conventional blade-type. Furthermore, the line representing the total
 581 energy of impact is plotted and compared with damage energy curve obtained for both the blade-types. It
 582 can be observed that overall, only 7-20% of the impact energy is absorbed as damage in the blade. This is
 583 in line with the discussion presented before where it was mentioned that most of the energy due to impact
 584 dissipated as elastic strain energy by means of rigid-body motions as well as rotations of the blade, with
 585 less energy being dissipated as damage in the blade. Nevertheless, the dissipated energy is sufficient to
 586 cause damage in the blade, which is mostly concentrated in the impact region locally. Furthermore, these

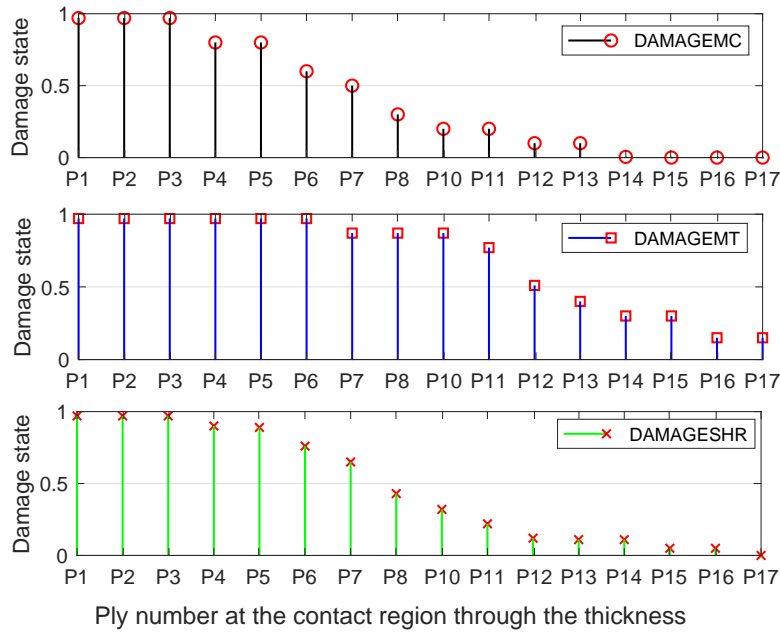


Figure 27: Ply wise (P) damage state at the contact region of the conventional blade-type

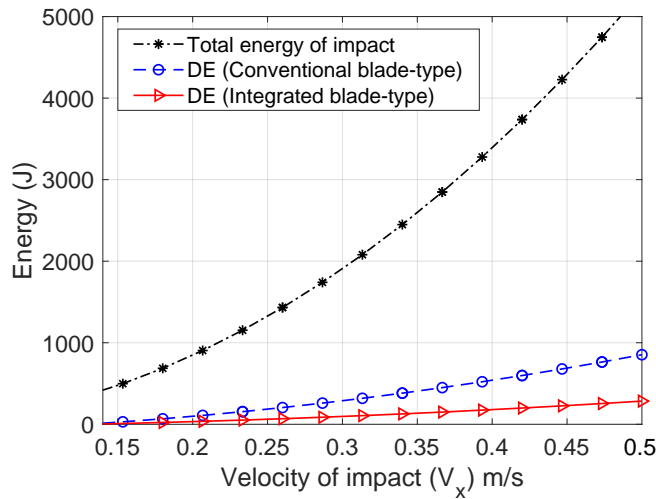


Figure 28: Comparison of damage energy (DE) with total energy of impact

587 results where majority of impact energy dissipates as rigid body motions highlights the requirement of
 588 advanced installation equipments like active tugger lines and guide wires, to prevent the risk of successive
 589 impact of the blade with nearby structures.

590 **5. Concluding remarks**

591 (1). The current study comprehensively investigated the impact behaviour of an offshore wind turbine
592 blade due to the impact with tower during lifting operation. It was mentioned that the lifting operations
593 using floating crane vessels is critical and can cause impact of the lifted blade with surrounding structures.
594 This can develop complex damage modes in the blades, capable of affecting their structural integrity.

595 (2). For planning blade lifting task, structural response-based operational limits are necessary. The
596 methodology from [6], includes a step which deals with the finite element analysis of the blade to investigate
597 its impact behaviour for different contact scenarios. Several parameters which determine impact/contact
598 scenario for the lifted blade during installation were identified. One of the identified parameters was the
599 design details of the blade being installed and was considered critical from structural perspective.

600 (3). An impact scenario was chosen for impact investigation in which the blade during the lift off
601 phase impacts the tower with its leading edge. The capability of shell-element based numerical modelling
602 technique was explored in Abaqus/Explicit. The discussion with respect to the impact dynamics, energy
603 evolutions and damage assessment in the blade was made. Two distinct blade-types (integrated blade-
604 type and conventional blade-type), two impact locations (contact region A and B) and different impact
605 velocities in the range of 0.02 m/s to 0.5 m/s were considered. Contact region A corresponds to the region
606 of the leading edge close to the yoke ($0.44 < r/R < 0.48$) whereas the contact region B corresponds to the
607 area near the tip of the blade ($0.68 < r/R < 0.71$).

608 (4). The results for the impact dynamics and motion of the blade after the impact were compared for
609 contact regions A and B. It was found that for the case in which the blade impacts the tower at contact
610 region A, there was significant development of internal energy along with large contact forces developed
611 in the blade compared to contact region B. Furthermore, the motion of the blade after impact varied for
612 the two different regions; rotation of the blade after the impact was dominant for contact region B, in
613 contrast to vibration in the blade for contact region A.

614 (5). Damage assessment results were presented for different impact velocities ranging from 0.02 m/s
615 to 0.5 m/s for both blade types. For the case of an integrated blade-type, most of the damage was
616 concentrated at the plies lying at the impact side. Furthermore, there was a smaller damage area, with
617 most of the energy absorbed by the core of the section. On the other hand, for the case of the conventional
618 blade-type, significant damage occurred for all the plies through the thickness, with damage spreading
619 over a larger area in the composite plies. Thus, there was significantly greater damage for the same impact
620 energy for the case of the conventional blade-type compared to the integrated blade-type.

621 (6). The dependences of the damage energy (DE) on the impact velocity (V_x) for both blade types
622 were established and compared with the total energy of impact. Most of the energy due to impact

623 dissipated as recoverable elastic strain energy by means of rigid-body motions and rotation of the blade,
624 with only 7-20% being dissipated as damage energy. Thus, designing advanced installation equipment,
625 such as active tugger lines and guide wires, is necessary to prevent the risk of successive impacts during
626 blade installation.

627 **6. Limitation and future work**

628 In the current work, shell-element based modelling method is utilised to investigate the impact be-
629 haviour of an offshore wind turbine blade due to impact loads during installation. The modelling method
630 is found efficient in predicting impact responses, and impact dynamics. In addition, the energy evolution
631 results complimented the discussions for damage assessment quite closely. However, as mentioned, the
632 shell-element based method could not capture delaminations in the composite plies and is limited when it
633 comes to predicting the crushing and inelastic deformations of the core in the thickness directions. These
634 limitations can affect the damage tolerance aspect of impact investigations in which the residual strength
635 analysis of the damaged blade is investigated. Therefore, global-local modelling methods need to be in-
636 vestigated to model delamination and core crushing at the leading edge, which have not been captured in
637 this study. Further, the analytical relationship between the damage energy and impact velocity needs to
638 be updated once the energy dissipated due to delamination of the plies is analysed. Again, it will be ideal
639 to perform experiments with impact loads on a real wind turbine blade. This will help in the validation of
640 numerical results and in a more explicit understanding of the impact-induced failure modes in the blade.

641

642 **Acknowledgment**

643 The work is supported by SFI MOVE projects and funded by Research Council of Norway, NFR project
644 number 237929. The authors also appreciate the anonymous reviewers for their valuable suggestions and
645 comments that helped to improve the quality of the work.

References

- [1] A. Ho, A. Mbistova, G. Corbetta, The european offshore wind industry-key trends and statistics 2016, Report, The European Wind Energy Association (EWEA) (2017).
- [2] L. Li, Dynamic Analysis of the Installation of Monopiles for Offshore Wind Turbines, PhD Thesis, NTNU (2016).

- [3] W. I. G. Acero, Assessment of Marine Operations for Offshore Wind Turbine Installation with Emphasis on Response-Based Operational Limits, PhD Thesis, NTNU (2016).
- [4] A. S. Verma, N. P. Vedvik, Z. Gao, Numerical assessment of wind turbine blade damage due to contact/impact with tower during installation, 276(1), IOP Conference Series: Materials Science and Engineering (2017).
- [5] L. Kuijken, Single Blade Installation for Large Wind Turbines in Extreme Wind Conditions, Master Thesis, Technical University of Denmark (2015).
- [6] A. S. Verma, Y. Zhao, N. P. Vedvik, Z. Gao, Explicit structural response-based methodology for assessment of operational limits for single blade installation for offshore wind turbines, 4th ICOE2018, Springer Publications (2018).
- [7] A. S. Verma, P. U. Haselbach, N. P. Vedvik, Z. Gao, A global-local damage assessment methodology for impact damage on offshore wind turbine blades during lifting operations, in: ASME 2018 37th International Conference on Ocean, Offshore and Arctic Engineering, American Society of Mechanical Engineers, 2018, pp. V010T09A064–V010T09A064.
- [8] A. S. Verma, Z. Jiang, N. P. Vedvik, Z. Gao, Z. Ren, Impact assessment of a wind turbine blade root during an offshore mating process, Accepted in Engineering Structures (2018).
- [9] https://www.siemens.com/press/en/events/2012/energy/2012_09-london.php, Picture.
- [10] <http://www.shipseller.net/details.php?id=1375>, Picture.
- [11] N. Baldock, F. Sevilla, R. Redfern, A. Storey, A. Kempenaar, C. Elkinton, Optimization of installation, operation and maintenance at offshore wind projects in the us, Tech. rep., Garrad Hassan America, Inc., San Diego, CA (United States) (2014).
- [12] S. Agrawal, K. K. Singh, P. Sarkar, Impact damage on fibre-reinforced polymer matrix composite—a review, Journal of Composite Materials 48 (3) (2014) 317–332.
- [13] S. Abate, Impact on composite structures, Cambridge university press, 2005.
- [14] M. McGugan, G. Pereira, B. F. Sørensen, H. Toftegaard, K. Branner, Damage tolerance and structural monitoring for wind turbine blades, Phil Trans R Soc A 373 (2035).
- [15] G. Perillo, J. Jørgensen, Numerical/experimental study of the impact and compression after impact on gfrp composite for wind/marine applications, Procedia Engineering 167 (2016) 129–137.

- [16] P. Haselbach, R. Bitsche, K. Branner, The effect of delaminations on local buckling in wind turbine blades, *Renewable Energy* 85 (2016) 295–305.
- [17] B. Hayman, Approaches to damage assessment and damage tolerance for frp sandwich structures, *Journal of Sandwich Structures & Materials* 9 (6) (2007) 571–596.
- [18] P. Haselbach, Ultimate Strength of Wind Turbine Blades under Multiaxial Loading, PhD Thesis, DTU Wind Energy (2015).
- [19] Y. Zhao, Z. Cheng, Z. Gao, P. C. Sandvik, T. Moan, Numerical study on the feasibility of offshore single blade installation by floating crane vessels. (revision submitted), *Marine Structures*.
- [20] C. Bak, F. Zahle, R. Bitsche, T. Kim, A. Yde, L. C. Henriksen, M. H. Hansen, A. Natarajan, Description of the DTU 10 MW Reference Wind Turbine, Progress report Report-I-0092, DTU Wind Energy (2013).
- [21] S. P. Rajbhandari, M. L. Scott, R. Thomson, D. Hachenberg, An approach to modelling and predicting impact damage in composite structures, *ICAS Congress* (2002) 8–13.
- [22] L. Sutherland, A review of impact testing on marine composite materials: Part I—Marine impacts on marine composites, *Composite Structures* (2017).
- [23] E. J. Barbero, Finite element analysis of composite materials using AbaqusTM, CRC press, 2013.
- [24] J. N. Reddy, Mechanics of laminated composite plates and shells: theory and analysis, CRC press, 2004.
- [25] H. Hibbit, B. Karlsson, P. Sorensen, Abaqus analysis users manual version 2016.
- [26] A. S. Verma, N. P. Vedvik, P. U. Haselbach, Z. Gao, Z. Jiang, Comparison of numerical modelling techniques for impact investigation on a wind turbine blade, *Composite Structures* 209 (C) (2019) 856–878.
- [27] P. P. Camanho, C. G. Dávila, Mixed-mode decohesion finite elements for the simulation of delamination in composite materials.
- [28] P. P. Camanho, C. G. Davila, M. De Moura, Numerical simulation of mixed-mode progressive delamination in composite materials, *Journal of composite materials* 37 (16) (2003) 1415–1438.
- [29] Z. Hashin, Failure criteria for unidirectional fiber composites, *Journal of applied mechanics* 47 (2) (1980) 329–334.

- [30] W. Weijermars, Mechanical behaviour of composite sandwich panels in bending after impact, MS Thesis, University of Twente., Enschede, Netherlands (2016).
- [31] N. Nanami, Structural and damage assessment of multi-section modular hybrid composite wind turbine blade, PhD Thesis, Texas A and M University (2014).
- [32] M. Vural, G. Ravichandran, Microstructural aspects and modeling of failure in naturally occurring porous composites, Mechanics of Materials 35.
- [33] S. Kadam, Failure criteria for evaluating strength of adhesive joints, Master Thesis, Delft university of technology (2014).
- [34] B. Xu, Fracture mechanisms and failure criteria of adhesive joints and toughened epoxy adhesives, PhD Thesis, Queen Mary, University of London (2010).
- [35] H. Özer, Ö. Öz, The use of the exponential drucker-prager material model for defining the failure loads of the mono and bi-adhesive joints, International Journal of Adhesion and Adhesives 76 (2017) 17–29.
- [36] <http://www.huntsman.com>, Araldite 2015-1 structural adhesives data sheet.